

# The PROSPECT Physics Program

J. Ashenfelter,<sup>1</sup> B. Balantekin,<sup>2</sup> H. R. Band,<sup>1</sup> G. Barclay,<sup>3</sup> C. D. Bass,<sup>4</sup> D. Berish,<sup>5</sup> N. S. Bowden,<sup>6</sup> A. Bowes,<sup>7</sup> C. D. Bryan,<sup>3</sup> J. P. Brodsky,<sup>6</sup> J. J. Cherwinka,<sup>8</sup> R. Chu,<sup>9,10</sup> T. Classen,<sup>6</sup> K. Commeford,<sup>11</sup> D. Davee,<sup>12</sup> D. Dean,<sup>9</sup> G. Deichert,<sup>3</sup> M. V. Diwan,<sup>13</sup> M. J. Dolinski,<sup>11</sup> J. Dolph,<sup>13</sup> J. K. Gaison,<sup>1</sup> A. Galindo-Uribarri,<sup>9,10</sup> K. Gilje,<sup>7</sup> A. Glenn,<sup>6</sup> B. W. Goddard,<sup>11</sup> M. Green,<sup>9</sup> K. Han,<sup>1</sup> S. Hans,<sup>14</sup> K. M. Heeger,<sup>1</sup> B. Heffron,<sup>9,10</sup> D. E. Jaffe,<sup>13</sup> D. Jones,<sup>5</sup> T. J. Langford,<sup>1</sup> B. R. Littlejohn,<sup>7</sup> D. A. Martinez Caicedo,<sup>7</sup> R. D. McKeown,<sup>12</sup> M. P. Mendenhall,<sup>15</sup> P. Mueller,<sup>9</sup> H. P. Mumm,<sup>15</sup> J. Napolitano,<sup>5</sup> R. Neilson,<sup>11</sup> D. Norcini,<sup>1</sup> D. Pushin,<sup>16</sup> X. Qian,<sup>13</sup> E. Romero,<sup>9,10</sup> R. Rosero,<sup>14</sup> B. S. Seilhan,<sup>6</sup> R. Sharma,<sup>13</sup> S. Sheets,<sup>6</sup> P. T. Surukuchi,<sup>7</sup> R. L. Varner,<sup>9</sup> B. Viren,<sup>13</sup> W. Wang,<sup>17,12</sup> B. White,<sup>9</sup> C. White,<sup>7</sup> J. Wilhelmi,<sup>5</sup> C. Williams,<sup>9</sup> T. Wise,<sup>1</sup> H. Yao,<sup>12</sup> M. Yeh,<sup>14</sup> Y.-R. Yen,<sup>11</sup> G. Zangakis,<sup>5</sup> C. Zhang,<sup>13</sup> and X. Zhang<sup>7</sup>  
(The PROSPECT Collaboration)

<sup>1</sup>Wright Laboratory, Department of Physics, Yale University, New Haven, CT, USA

<sup>2</sup>Department of Physics, University of Wisconsin, Madison, Madison, WI, USA

<sup>3</sup>High Flux Isotope Reactor, Oak Ridge National Laboratory, Oak Ridge, TN, USA

<sup>4</sup>Department of Chemistry and Physics, Le Moyne College, Syracuse, NY, USA

<sup>5</sup>Department of Physics, Temple University, Philadelphia, PA, USA

<sup>6</sup>Nuclear and Chemical Sciences Division, Lawrence Livermore National Laboratory, Livermore, CA, USA

<sup>7</sup>Department of Physics, Illinois Institute of Technology, Chicago, IL, USA

<sup>8</sup>Physical Sciences Laboratory, University of Wisconsin, Madison, Madison, WI, USA

<sup>9</sup>Physics Division, Oak Ridge National Laboratory, Oak Ridge, TN, USA

<sup>10</sup>Department of Physics and Astronomy, University of Tennessee, Knoxville, TN, USA

<sup>11</sup>Department of Physics, Drexel University, Philadelphia, PA, USA

<sup>12</sup>Department of Physics, College of William and Mary, Williamsburg, VA, USA

<sup>13</sup>Physics Department, Brookhaven National Laboratory, Upton, NY, USA

<sup>14</sup>Chemistry Department, Brookhaven National Laboratory, Upton, NY, USA

<sup>15</sup>National Institute of Standards and Technology, Gaithersburg, MD, USA

<sup>16</sup>Institute for Quantum Computing and Department of Physics, University of Waterloo, Waterloo, ON, Canada

<sup>17</sup>School of Physics and Engineering, Sun Yat-Sen University, Guangzhou, Guangdong Province, China

The Precision Reactor Oscillation and Spectrum Experiment, PROSPECT, is designed to make a precise measurement of the antineutrino spectrum from a highly-enriched uranium reactor and probe eV-scale sterile neutrinos by searching for neutrino oscillations over meter-long distances. PROSPECT is conceived as a 2-phase experiment utilizing segmented <sup>6</sup>Li-doped liquid scintillator detectors for both efficient detection of reactor antineutrinos through the inverse beta decay reaction and excellent background discrimination. PROSPECT Phase I consists of a movable 3-ton antineutrino detector at distances of 7–12 m from the reactor core. It will probe the best-fit point of the  $\nu_e$  disappearance experiments at  $4\sigma$  in 1 year and the favored region of the sterile neutrino parameter space at  $>3\sigma$  in 3 years. With a second antineutrino detector at 15–19 m from the reactor, Phase II of PROSPECT can probe the entire allowed parameter space below  $10 \text{ eV}^2$  at  $5\sigma$  in 3 additional years. The measurement of the reactor antineutrino spectrum and the search for short-baseline oscillations with PROSPECT will test the origin of the spectral deviations observed in recent  $\theta_{13}$  experiments, search for sterile neutrinos, and conclusively address the hypothesis of sterile neutrinos as an explanation of the reactor anomaly.

Contents		Neutrinos: Complementarity and Discovery Reach	
I. Executive Summary and Background	2	III. PROSPECT Physics Program and Discovery Potential	7
A. The Reactor Antineutrino Anomaly	3	A. Sensitivity to Short-Baseline Neutrino Oscillation	8
B. Reactor Spectrum Anomaly	4	B. Precision Measurement of the Reactor $\bar{\nu}_e$ Spectrum	10
C. Anomalies in Source and Accelerator Experiments	5	C. Reactor Monitoring and Characterization	11
D. Global Fits	5		
E. Implications for the Future Neutrino Program	6	IV. PROSPECT Experimental Strategy	11
II. Worldwide Program to Search for Sterile		A. Reactor Site	11

B. Antineutrino Detector Design and Performance	11
C. Calibration Strategy	12
D. Research and Development Status	13
1. Reactor Facility Background Measurements	13
2. Liquid Scintillator Development	14
3. Detector Prototyping	15
4. Onsite Prototype Detector Operation and Simulation Validation	15
E. Timeline	17
V. Predicted Detector Response: Signal and Background	17
A. Response to the Reactor $\bar{\nu}_e$ Signal	17
B. Backgrounds from Cosmogenic Activity	17
C. Backgrounds from Internal Radioactivity	19
VI. Conclusions	19
VII. Acknowledgements	20
References	20

## I. Executive Summary and Background

Recent neutrino experiments have provided a coherent picture of neutrino flavor change and mixing and allowed the precise determination of oscillation parameters in the 3-neutrino model. However, anomalous results in the measurement of the reactor  $\bar{\nu}_e$  spectrum and flux have suggested this picture is incomplete and may be interpreted as indicators of new physics. Reactor  $\bar{\nu}_e$  experiments observe a  $\sim 6\%$  deficit in the absolute flux when compared to predictions [1, 2]. The observed flux deficit, the “reactor antineutrino anomaly”, has led to the hypothesis of oscillations involving a sterile neutrino state with  $\sim 1$  eV<sup>2</sup> mass splitting [3–5] (Fig. 1). Moreover, measurements of the reactor  $\bar{\nu}_e$  spectrum by recent  $\theta_{13}$  experiments indicate spectral discrepancies compared to predictions, particularly at  $\bar{\nu}_e$  energies of 4–7 MeV [6–8] (Fig. 2). The reactor anomaly and the measured spectral deviations are open issues in a suite of anomalous results [4] that may hint at revolutionary new physics in the neutrino sector.

The Precision Reactor Oscillation and Spectrum Experiment, PROSPECT [9], is designed to comprehensively address this situation by making a definitive search for  $\bar{\nu}_e$  oscillations at short baselines from a compact reactor core while concurrently making the world’s most precise  $\bar{\nu}_e$  energy spectrum measurement from a highly-enriched uranium (HEU) research reactor. By simultaneously measuring the relative  $\bar{\nu}_e$  flux and spectrum at multiple distances from the core within the same detector, PROSPECT will probe for oscillations into additional neutrino states in the parameter

space favored by reactor and radioactive source experiments independent of any reactor model predictions. PROSPECT covers a unique region of parameter space at the eV<sup>2</sup>-scale that is complementary to current  $\bar{\nu}_e$  disappearance limits from Daya Bay and to  $\nu_\mu$  and  $\nu_e$  oscillation searches in accelerator-based neutrino oscillation experiments. Together, reactor and accelerator experiments define a comprehensive approach to resolving the current anomalous results in neutrino physics and have the potential to make a paradigm-changing discovery. Observation of an eV-scale sterile neutrino would have a profound impact on our understanding of neutrino physics and the Standard Model of particle physics with wide-ranging implications for the physics reach of the planned US long-baseline experiment DUNE [10], searches for neutrinoless double beta decay, neutrino mass constraints from cosmology and beyond.

By making a high-resolution energy spectrum measurement, PROSPECT will also determine if the observed spectral deviations in Daya Bay and other  $\theta_{13}$  experiments at commercial nuclear power plants persist in a HEU research reactor and provide a precision benchmark spectrum to test the modeling of reactor  $\bar{\nu}_e$  production. A better understanding of the reactor  $\bar{\nu}_e$  spectrum will aid precision medium-baseline reactor experiments such as JUNO and RENO-50 [11], and improve reactor monitoring capabilities for nonproliferation and safeguards.

The goals of the PROSPECT experiment are to:

- Make an unambiguous discovery of eV-scale sterile neutrinos through the observations of energy and baseline dependent oscillation effects, or exclude the existence of this particle in the allowed parameter region with high significance. Accomplishing this addresses the proposed sterile neutrino explanation of the reactor anomaly using a method that is independent of reactor flux predictions;

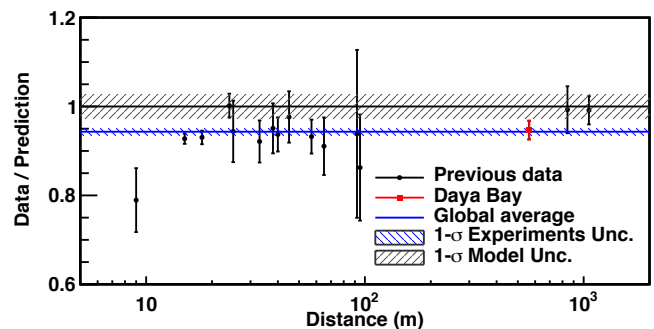


FIG. 1. Comparison of measured reactor antineutrino fluxes with predictions based on models for the emission of reactor antineutrinos. The measured deficit relative to prediction is known as the “reactor antineutrino anomaly” [3]. Fig. 1 from [6].

- Directly test reactor antineutrino spectrum predictions using a well-understood and modeled reactor system, while also providing information that is complementary to nuclear data measurement efforts;
- Demonstrate techniques for antineutrino detection on the surface with little overburden;
- Develop technology for use in nonproliferation applications.

PROSPECT will employ a phased approach for the timely exploration of the favored parameter space with the potential of a high-impact discovery while preparing for a definitive measurement across the entire allowed parameter region. PROSPECT will be located at the High Flux Isotope Reactor (HFIR) [12] at Oak Ridge National Laboratory (ORNL) [13]. The proposed layout of the experiment is shown in Fig. 3. Phase I of PROSPECT consists of a  $\sim 3$ -ton, segmented  $^6\text{Li}$ -doped liquid scintillator antineutrino detector (AD-I) accessing baselines in the range 7–12 m from the reactor core. Phase II involves the addition of a second  $\sim 10$ -ton antineutrino detector (AD-II) with identical segmentation spanning baselines between 15–19 m.

PROSPECT combines competitive exposure, baseline mobility for increased physics reach and systematic checks, good energy and position resolution, and efficient background discrimination that yields a signal over background sufficient to achieve stated goals. The additional second detector in Phase II will allow PROSPECT to become the most sensitive experiment

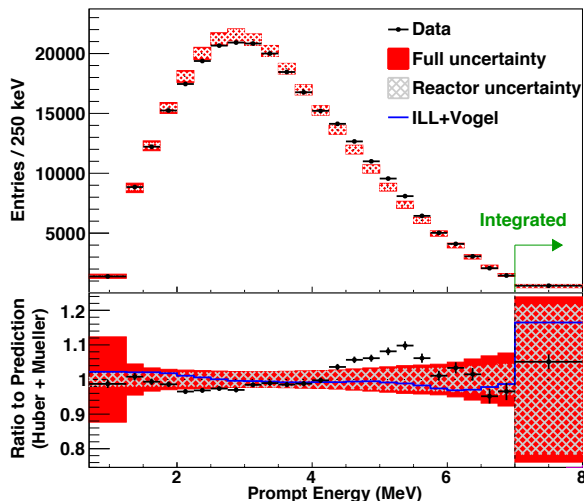


FIG. 2. Comparison of the measured antineutrino energy spectra from pressure water reactors (PWR) to modern models for reactor neutrino emission observed in the Daya Bay experiment (Fig. 2 from [6]). The deviation from prediction between 4–6 MeV, which is also observed in two other similar experiments, is unexplained and may indicate deficiencies in the models and/or the nuclear data underlying them.

of all proposed reactor-based short-baseline searches. Within a single calendar year, PROSPECT Phase I can probe the best-fit region for all current global analyses of  $\nu_e$  and  $\bar{\nu}_e$  disappearance [4, 5] at  $4\sigma$  confidence level. Over 3 years of operation, PROSPECT Phase I can discover oscillations as a sign of sterile neutrinos at  $5\sigma$  for the best-fit point and  $3\sigma$  over the majority of the suggested parameter space. After 3 additional years of operation with a second antineutrino detector in Phase II, essentially all parameter space suggested by  $\nu_e$  disappearance data below  $10 \text{ eV}^2$  can be excluded at  $5\sigma$ .

### A. The Reactor Antineutrino Anomaly

Recent atmospheric, solar, reactor, and accelerator experiments have established the framework of neutrino mixing and flavor change and determined related neutrino oscillation parameters. Reactor experiments have utilized the inverse beta decay interaction to detect  $\bar{\nu}_e$  emitted by beta decays of fission daughter products and measure the flux and spectrum of reactor  $\bar{\nu}_e$  over a range of distances from reactors. Prior to the discovery of neutrino oscillations, experiments positioned  $< 100$  m from a variety of reactor cores, including those at ILL-Grenoble, Bugey, and Savannah River, measured the flux of  $\bar{\nu}_e$  with ton-scale detectors based on liquid scintillators and/or  $^3\text{He}$  proportional counters [14–22]. These results were in good agreement with contemporary predictions based on conversion of  $\beta^-$  spectra of fissioning isotopes measured at the ILL-Grenoble research reactor [23, 24].

Motivated by experiments seeking to measure  $\theta_{13}$ , an improved prediction of the reactor  $\bar{\nu}_e$  flux was performed [1] using a novel approach combining *ab-initio* and conversion methods, incorporating updated nuclear data, and more accurate nuclear corrections. The summation, or *ab-initio*, portion of the prediction built the  $\bar{\nu}_e$  spectrum from the sum of daughter products contributions for which fission yield, branching ratio, and decay information were available from nuclear databases, allowing nuclear corrections to be applied at the branch level. The residual  $\sim 10\%$  of the spectrum was derived via a conversion procedure using the reference ILL  $\beta^-$  spectrum [23–26]. The residual contribution to the total  $\beta^-$  spectra from fission daughter products isotopes without nuclear data was fit using five virtual  $\beta$ -branches, where importantly and in contrast to past prediction methods, corrections were applied at the branch level. The  $\bar{\nu}_e$  spectrum obtained following this approach, when combined with the inverse beta decay cross section, resulted in a systematic increase in the detectable reactor  $\bar{\nu}_e$  flux. Note that this increase is due to the improved evaluation resulting in a greater proportion of the emitted  $\bar{\nu}_e$  being above the threshold for inverse beta decay – the total  $\bar{\nu}_e$  flux is still anchored to the normalization of the ILL  $\beta^-$  measurement. In conjunction with the revision of the neutron mean life-

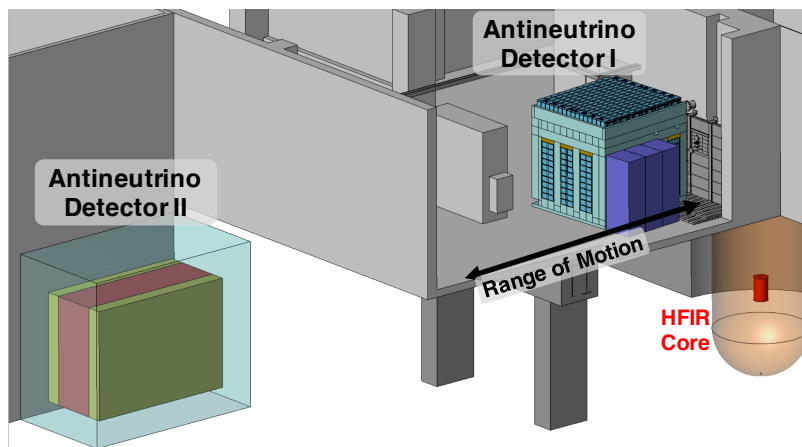


FIG. 3. Layout of the PROSPECT experiment. Shown are the HFIR reactor core and the two antineutrino detectors, AD-I and AD-II. Phase I consists of a movable antineutrino detector, AD-I, operated for three years at a baseline range of 7–12 m. Phase II adds a  $\sim 10$ -ton detector, AD-II, at 15–19 m for an extra three years of data taking.

time [27], this effect results in an average deficit of 5.7% in all the short-baseline reactor  $\bar{\nu}_e$  measurements. This discrepancy between data and prediction, referred to as the “reactor antineutrino anomaly” [3], represents a deficit in the ratio of observed to expected  $\bar{\nu}_e$  from unity significant at 98.6% confidence level.

An independent cross-check was performed using an approach based only on an improved conversion of the ILL reference  $\beta^-$  spectrum, which minimized the use of nuclear databases [2]. Virtual  $\beta$ -branches were used to convert the ILL reference to an  $\bar{\nu}_e$  spectrum, yielding a net increase of  $\sim 6\%$  in antineutrino predictions, consistent with the flux predicted in [1]. The cause of the increase relative to past predictions was also understood to be due to the use of improved nuclear corrections, the updated neutron lifetime, and the application of corrections to the beta decay spectrum at the branch level, in contrast to the “effective” correction used in past predictions. Additionally, blind analyses from recent kilometer baseline precision rate measurements are consistent with the previous reactor experiments [6–8]. The disagreement between modern reactor  $\bar{\nu}_e$  flux predictions and measurement is therefore well-established.

Oscillations at short baselines due to a new type of neutrino with a mass splitting of  $\Delta m^2 \sim 1 \text{ eV}^2$  have been proposed as one explanation for these observations [3]. With invisible decay width results from Z boson measurements stringently limiting the number of active neutrino flavors to three [27], any additional existing neutrino should be ‘sterile’ and not participate in weak interactions. The oscillation arising from such a neutrino with eV-scale mass splitting can be observed at baselines around 10 m from a compact reactor core.

Deficiencies in the flux prediction methods and/or imperfections in the measured data underlying them should also be considered as an explanation for the “reactor anomaly.” For example, incomplete nuclear data

for the beta decays contributing to the reactor spectrum as well as uncertainties in the corrections applied to individual beta spectra may lead to significant uncertainties in the conversion procedure between the reference beta electron and the emitted  $\bar{\nu}_e$  spectra [28]. Observed spectral discrepancies in addition to the flux deficit, as described in the next section, highlight this concern. More data is needed to understand and explain these observations. PROSPECT can address both of these possibilities through a high precision spectral measurement in addition to an oscillation search for sterile neutrinos, and therefore provide a comprehensive solution to the present “reactor anomalies.”

## B. Reactor Spectrum Anomaly

Neutron-rich fission fragments within a reactor emit  $\bar{\nu}_e$  via beta decay with an energy spectrum dependent on the transition between initial and final nuclear states of the particular isotope. The total energy spectrum  $S(E_{\bar{\nu}})$  can be expressed as a sum of the decay rate of each unstable isotope  $i$  in the reactor,  $R_i$ , times the branching fraction for beta decay  $f_{ij}$  to the nuclear state  $j$  with an energy spectrum  $S_{ij}(E_{\bar{\nu}})$ ,

$$S(E_{\bar{\nu}}) = \sum_i R_i \sum_j f_{ij} S_{ij}(E_{\bar{\nu}}). \quad (1)$$

While this calculation is straightforward in principle, it is complex in practice. More than 1000 unstable isotopes contribute, and many fission yields and individual beta decay spectra are poorly known. For those measured, there can still be significant uncertainty in the decay levels, branching fractions, and  $\bar{\nu}_e$  energy spectra. It has recently been demonstrated that the two major nuclear databases, ENDF and JEFF,

contain differences in branching fractions [29], complicating the interpretation of these calculations. Separately, total-absorption gamma spectroscopy measurements of key isotopes have shown that quoted uncertainties are frequently underestimated [30]. Consequently, *ab-initio* calculations of  $S(E_{\bar{\nu}})$  are thought accurate to only  $\sim 10\%$  [28].

Given the uncertainties in this approach, the conversion method has become the de-facto standard for modeling reactor  $\bar{\nu}_e$  energy spectra. The cumulative  $\beta^-$  energy spectra emitted by foils of fissioning material were measured [23–26, 31] and used to estimate the corresponding cumulative  $\bar{\nu}_e$  spectra with an estimated uncertainty at the few-percent level. As described in Sec. IA however, modern predictions of this type disagree with measurements of the flux, leading to the reactor antineutrino anomaly. In addition, recent, high-precision measurements of the antineutrino energy spectrum from  $\theta_{13}$  experiments have shown deviations from the theoretically predicted spectral shapes. The measured spectra from Daya Bay, Double Chooz, and RENO each show an excess of antineutrinos of approximately 10% with energies between 5 and 7 MeV [6–8].

Initial studies indicated that the *ab-initio* method reproduced the shape of the spectrum better than the beta-conversion predictions [32]. However, re-analyses with updated fission and beta-branch information call this result into question and instead point to antineutrinos produced by the  $^{238}\text{U}$  fission chain as a possible source of the spectral anomaly [29]. New measurements with total-absorption gamma spectrometers at ORNL [33] and University of Jyväskylä [30] will reduce uncertainties in individual beta-decay levels and branching ratios. However, predicting antineutrino spectra resulting from these decays remains challenging due to unknown shape corrections. Similarly, uncertainties in the cumulative fission yields are not addressed by these measurements. Precision measurements of reactor antineutrino spectra provide a unique experimental probe that can address many of these questions [29]. In particular, a first-ever precision measurement of the  $^{235}\text{U}$  spectrum would highly constrain predictions for a static single fissile isotope system, as compared to commercial power reactors that have evolving fuel mixtures of multiple fissile isotopes.

### C. Anomalies in Source and Accelerator Experiments

Anomalous results have also been obtained in other neutrino experiments. Both the SAGE and GALLEX radiochemical experiments have observed neutrino flux deficits with high-activity  $\nu_e$  calibration sources [34–37].

Additional anomalies have become apparent in accelerator-based neutrino experiments. The Liquid Scintillator Neutrino Detector (LSND) Experiment at Los Alamos National Laboratory was designed to

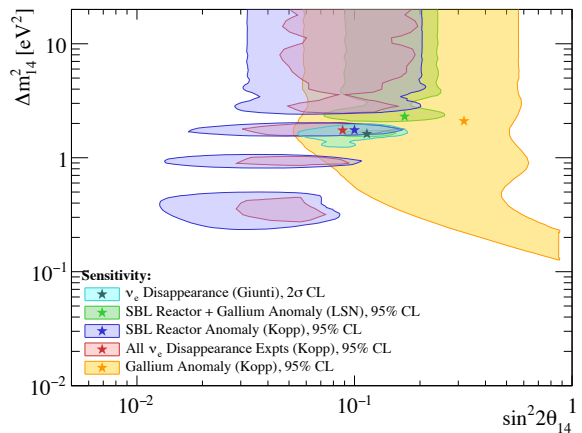


FIG. 4. Allowed regions in 3+1 framework for several combinations of  $\nu_e$  and  $\bar{\nu}_e$  disappearance experiments. Contours obtained from [3, 5, 40].

search for neutrino oscillations in the  $\bar{\nu}_\mu \rightarrow \bar{\nu}_e$  channel. It measured an excess of events at low energy consistent with an oscillation mass splitting of  $|\Delta m^2| \sim 1 \text{ eV}^2$  [38]. The Mini Booster Neutrino Experiment (MiniBooNE) at Fermilab was conceived to test this so-called “LSND anomaly” in the same L/E region [39]. In both the  $\bar{\nu}_\mu \rightarrow \bar{\nu}_e$  and  $\nu_\mu \rightarrow \nu_e$  appearance channels, it observed an excess of events. There is some disagreement regarding the compatibility of MiniBooNE  $\bar{\nu}_e$  appearance data in models involving 3 active neutrinos and 1 sterile state (3+1 model) [40] but the allowed regions for neutrino oscillations partially overlap with the allowed regions from LSND.

### D. Global Fits

Attempts have been made to fully incorporate the observed anomalies into a 3+1 framework of neutrino oscillations. Combining the short-baseline reactor anomaly data with the gallium measurements under the assumption of one additional sterile neutrino state allows one to determine the allowed regions ( $\Delta m^2_{14}$ ,  $\sin^2 2\theta_{14}$ ) in the global parameter space. Two recent efforts obtain slightly different allowed regions and global best-fit points [3, 5]. The disagreement can be attributed to the differences in handling uncertainties and the choice of spectral information included in the analyses. Inclusion of all  $\nu_e$  and  $\bar{\nu}_e$  disappearance measurements further constrains the parameter space [5]. Fig. 4 illustrates the allowed regions obtained from different combinations of anomalous experimental results.

Because of the tensions between some appearance and disappearance results, difficulties arise in developing a consistent picture of oscillations in the 3+1 framework [40] involving both appearance and disappearance data. Efforts at performing a global fit in frame-

works containing two additional sterile neutrinos have produced results that have only slightly better compatibility [5]. Excluding the MiniBooNE low-energy excesses yields allowed regions in a 3+1 framework and has been suggested [40] as a “pragmatic approach,” based on the observation that the MiniBooNE anomalies cannot be explained in any of the frameworks.

A short-baseline oscillation experiment sensitive to the phase space in  $\Delta m_{14}^2$  and  $\sin^2 2\theta_{14}$  suggested by  $\nu_e$  and  $\bar{\nu}_e$  global fits (see Fig. 4) will be able to conclusively address the  $\sim 1$  eV<sup>2</sup> sterile neutrino interpretation of these anomalous results.

### E. Implications for the Future Neutrino Program

The discovery of sterile neutrinos would be a profound result with far-reaching implications for nuclear and particle physics as well as cosmology. Sterile neutrinos would represent a new class of particles and possibly indicate non-standard interactions. An extension of the Standard Model would be required and our fundamental understanding of particles and interactions would change. The addition of sterile states would require an extension of the PMNS matrix describing neutrino mixing and have a dramatic impact on our interpretation of future neutrino experiments.

The Fermilab Long-Baseline Neutrino Facility (LBNF) and the Deep Underground Neutrino Experiment (DUNE) aim to make a precision measurement of neutrino oscillation with the goal of determining the mass hierarchy and the CP-violating phase. The existence of a single eV-scale sterile neutrino implies an additional mass eigenstate, which leads to 3 new mass splittings, mixing angles, and CP-violating phases that can alter the oscillation behavior of neutrinos over the 1300 km DUNE baseline. One or more sterile neutrino states would significantly impact the interpretation of the neutrino event rate and spectrum measured in DUNE.

Fig. 5 shows the expected rates of neutrinos and antineutrinos for DUNE in the standard three neutrino framework (3+0) and a 3+1 framework for three different combinations of mixing angles  $\theta_{14}$  and  $\theta_{24}$  and allowing the 3 CP-violating phases to vary from  $[-180^\circ, 180^\circ]$ . The difference in event rates between the 3+0 and 3+1 cases can lead to ambiguities in the interpretation of CP-violation searches and complicate the precision measurement of neutrino parameters in the DUNE experiment.

Neutrinoless double beta decay ( $0\nu\beta\beta$ ) experiments are probing the Majorana nature of neutrinos and may allow determination of the effective neutrino mass from the nuclear transition rate. Light sterile neutrinos can contribute to the  $0\nu\beta\beta$  decay rate [41] and thus alter the prediction of the effective neutrino Majorana mass  $m_{\beta\beta}$  significantly as shown in Fig. 6. In the 3+1 sterile neutrino model, the addition of sterile neutrino mass and

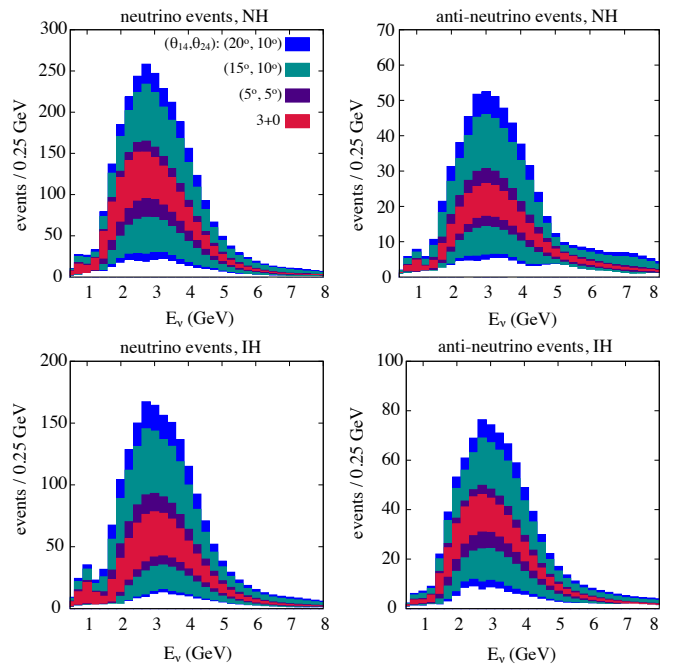


FIG. 5. Expected neutrino and antineutrino rates for DUNE as a function of reconstructed neutrino energy with and without sterile neutrinos, from [10]. Each band corresponds to the range of event rates possible for a particular case. In the 3+0 scenario labelled by the red band,  $\delta_{CP}$  is varied from  $[-180^\circ, 180^\circ]$ . For the 3+1 case, three sets of  $(\theta_{14}, \theta_{24})$  are represented: blue band  $(20^\circ, 10^\circ)$ , green band  $(15^\circ, 10^\circ)$ , purple band  $(5^\circ, 5^\circ)$ . Each set varies  $\theta_{34}$  from  $[0^\circ, 30^\circ]$  and CP-violating phases  $\delta_{13}$ ,  $\delta_{24}$ , and  $\delta_{34}$  from  $[-180^\circ, 180^\circ]$ .

mixing expands the allowed region for the inverted hierarchy and shifts the normal hierarchy space to higher values of  $m_{\beta\beta}$ . Next-generation, ton-scale  $0\nu\beta\beta$  experiments aim to probe this effective neutrino mass down to 15 meV [42]. With this sensitivity, experiments will search the entire allowed parameter space of the inverted hierarchy under the assumption of 3 active neutrinos. Both understanding the mass hierarchy and the existence of sterile neutrinos will be important for interpreting the parameter space probed by  $0\nu\beta\beta$  experiments.

The existence of light sterile neutrinos would impact neutrino mass measurements from beta decay and cosmological experiments. An eV-scale sterile neutrino mass term contributes to the effective electron neutrino mass  $m_\beta = \sum_i \sqrt{|U_{ei}^2 m_i^2|}$  and alters the spectrum shape measured in beta decay experiments. For this reason, sterile neutrinos may manifest itself in the Karlsruhe Tritium Neutrino (KATRIN) experiment, which can in turn probe the global parameter space in  $\Delta m_{14}^2$  and  $\sin^2 2\theta_{14}$  that is complementary to reactor experiments [43, 44].  $\Sigma m_\nu$  measured in cosmological experiments such as Planck [45] is also sensitive to the existence of sterile neutrinos. Based on current results, the

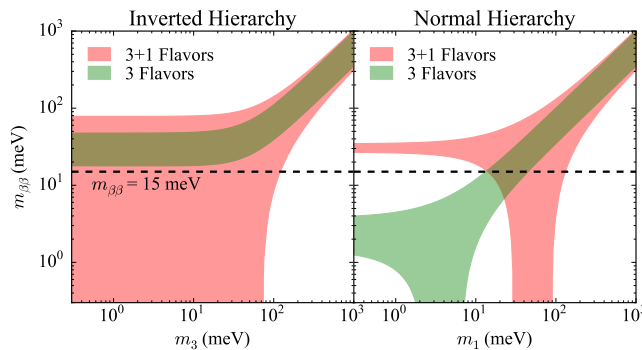


FIG. 6. The influence of sterile neutrinos on the effective neutrino mass  $m_{\beta\beta}$  accessible in neutrinoless double beta decay experiments for inverted hierarchy (left) and normal hierarchy (right) scenarios. The horizontal axis is lightest neutrino mass, i.e.  $m_3(m_1)$  for inverted (normal) hierarchy. The allowed region for 3+1 flavors (3 flavors) shown in red (green) are calculated with best-fitted 3-flavor oscillation parameters from [27]. Mixing parameters of the additional sterile flavor is from [5]. The dashed horizontal line indicates the targeted sensitivity for next-generation ton-scale neutrinoless double beta decay experiments.

observation of an eV-scale sterile neutrino in terrestrial experiments would be in tension with existing model-dependent cosmological limits and require additional model extensions such as sterile neutrino decay [46].

## II. Worldwide Program to Search for Sterile Neutrinos: Complementarity and Discovery Reach

Multiple experiments have been proposed to test the eV-scale sterile neutrino interpretation of the anomalous results described in Sec. IA and IC. These programs include observations of reactor  $\bar{\nu}_e$  [47–52], as well as  $\nu_e$  and  $\bar{\nu}_e$  from radioactive sources [53]. All must operate at short baselines of several meters from a strong neutrino source. This leads to a unique set of challenges, including near-surface backgrounds, source related backgrounds, and facility constraints on possible baselines and/or target mass. To understand the physics reach of the proposed short-baseline efforts, we briefly summarize the range of parameters and their impact on the sensitivity of the experiments.

With the exception of the source experiments using pre-existing, large neutrino detectors, all of the proposed reactor experiments will be composed of liquid or solid scintillator targets with fiducialized masses on the ton-scale. Exposures, defined as the “reactor power·detector mass·reactor live time”, are also similar for most next-generation detectors located  $\mathcal{O}(10)$  meters) from HEU reactor cores, ranging from  $\sim 40$ –157 MW·ton·year. PROSPECT Phase I will have an exposure of 157 MW·ton·year. As such, the difference in sensitivity between different experiments de-

pends on the baseline coverage, energy resolution, position resolution, and the signal-to-background (S:B) ratio. PROSPECT Phase II proposed to add a second detector with mass of  $\mathcal{O}(10)$  tons) that increases the oscillation sensitivity beyond the general sensitivity of ton-scale, short-baseline experiments. The second detector will greatly increase the reach in baseline and the accessible range of the characteristic  $L/E$  parameter for neutrino oscillations.

All but one of the proposed experiments will have the capability to probe distances of  $<10$  m from respective reactor cores maximizing both the  $\bar{\nu}_e$  interaction rate and sensitivity to meter-scale oscillations. However, only two of the eight reactor experiments, including PROSPECT, plan to vary the baseline with their ton-scale detector. In addition to improving the oscillation sensitivity, variable baseline coverage provides an important handle on detector systematic checks and background studies.

Good resolution in energy and position are required to make a measurement of the HEU spectrum, search for oscillations, and efficient background rejection. To test the observed spectral anomaly, an energy resolution of at least that obtained by the  $\theta_{13}$  experiments, 8% at 1 MeV, is ideal. PROSPECT aims to achieve  $4.5\%/\sqrt{E}$  which is sufficient to resolve spectral features associated with significant groups of decay branches, and thus inform modeling efforts. With a position resolution of 15 cm PROSPECT will be able to resolve any oscillation effects and perform an efficient rejection of dominant backgrounds from cosmogenic showers.

The signal-to-background in the detectors varies depending on reactor site and overburden, passive shielding, and background rejection capabilities. Some of the reactor experiments have done background studies at various reactor sites and in some cases coupled these with detailed Monte Carlo simulation. Sensitivities reported by each collaboration include the projected S:B, ranging from 1-3 at HEU sites and 5 at LEU sites. PROSPECT has done an extensive suite of background measurements [54] and data-benchmarked simulations that indicate an expected S:B ratio of  $>1$  as summarized in Table. I.

In addition to reactor experiments, short-baseline searches using intense beta decay sources can also search for oscillations in the disappearance channel. In particular, the CeSOX experiment plans to perform such a measurement with a 2-4 PBq  $^{144}\text{Ce}$ - $^{144}\text{Pr}$  source at a baseline of 7.15 m from the center of the Borexino detector at Gran Sasso Laboratory [53]. Antineutrinos will be detected via the inverse beta decay process and evidence of oscillations would be probed through measurement of either relative  $L/E$  distortion or deviations in the measured absolute rate and spectrum from predictions. Data will be taken for 1.5 years beginning in late 2016. This experiment will provide a sensitive probe of short-baseline oscillation, but source-related systematic estimates based on absolute activity

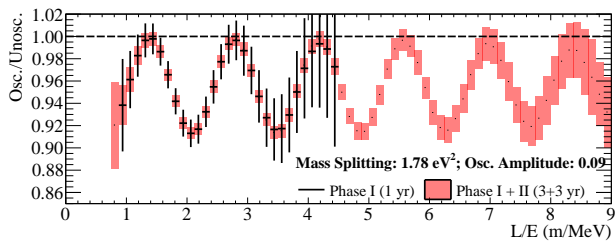


FIG. 7. Asymmetry between oscillated and un-oscillated  $L/E$  spectra after 1 year of Phase I (black) and 3 years of both Phase I+II for representative oscillation parameters.

measurement uncertainties and on neutrino spectrum shape factors will be challenging to produce. Run time and total statistics are limited for this experiment type by the 285 day half-life of the radioactive source.

The Short Baseline Neutrino (SBN) program [55], a consortium consisting of three detectors at varied distances from the accelerator neutrino source at Fermilab, aims to perform a relative oscillation search to resolve the LSND and MiniBooNE anomalies. While reactor experiments pursue oscillations in  $\bar{\nu}_e$  disappearance channel, SBN searches for hints of sterile neutrinos in  $\nu_e$  appearance channel in addition to providing a sensitive relative  $\nu_\mu$  disappearance analysis. The combined suite of experiments will help address all the relevant anomalies in the corresponding parameter space. Oscillation hints observed in one channel will suggest regions of focus for other channels. Conversely, a null oscillation result with significant confidence in all channels will conclusively rule out the existence of sterile neutrinos in the currently-suggested  $|\Delta m^2| \sim 1 \text{ eV}^2$  parameter space.

### III. PROSPECT Physics Program and Discovery Potential

#### A. Sensitivity to Short-Baseline Neutrino Oscillation

PROSPECT will perform a sensitive search for light sterile neutrinos at the eV mass scale by probing signatures of neutrino oscillation through a relative comparison of the reactor flux and spectrum across a range of baselines (Fig. 3). The experiment has been designed (Sec. IV) to provide significant improvements in baseline coverage, event statistics, and energy resolution over previous short-baseline reactor oscillation measurements, thus providing coverage of oscillation parameter space that was previously inaccessible.

To demonstrate the oscillation physics reach, we present sensitivity studies assuming the existence of one sterile neutrino in addition to the three known neutrino species, commonly referred to as the 3+1 model. We note that PROSPECT’s broad baseline range and in particular its extended reach in  $L/E$  during Phase II will also provide sensitivity to multiple sterile neutrinos [56]. The choice of many input parameters is informed by the PROSPECT R&D program. This includes

detailed information on the HFIR core, AD-I performance and background estimates obtained from simulation studies and test detector operation, and deployment locations based on engineering engagement with the HFIR facility.

PROSPECT will measure the relative  $\bar{\nu}_e$  flux and spectrum as a function of reconstructed baseline and can directly map out the oscillation effect within the segmented detectors [58]. This is shown in Fig. 7 for the single sterile neutrino hypothesis with parameters matching a global fit to  $\nu_e$  disappearance data (Ref. [5], hereafter referred to as “Kopp best-fit”). For this best-fit mass splitting, more than one full oscillation wavelength will be visible in PROSPECT Phase I due to the wide baseline and energy range covered. Extension of PROSPECT to Phase II accesses more oscillation cycles and adds statistical precision, thereby enhancing sensitivity. It should be emphasized that the oscillation measurement in the PROSPECT AD-I is a relative comparison between  $L/E$  bins rather than between the flux measured in each AD-I segment. Because the relative range of baselines spanned by AD-I is smaller than the  $\bar{\nu}_e$  energy range, each segment contributes to the majority of  $L/E$  bins and relative normalization plays a less important role in PROSPECT than near and far detector relative normalization does in the recent  $\theta_{13}$  experiments. Furthermore, as AD-I is moved, the relative contribution of each segment to a particular  $L/E$  bin varies, reducing the effect of both correlated and uncorrelated systematic biases more efficiently than a single extended detector.

PROSPECT oscillation sensitivity is determined using a  $\chi^2$  minimization [59]. Systematic uncertainties are included by minimizing over nuisance parameters in addition to the new oscillation parameters ( $\Delta m_{14}^2, \sin^2 2\theta_{14}$ ). We take a conservative approach of allowing uncertainties for these parameters to vary broadly with little penalty in the fit. Relative uncertainties in normalizations and uncorrelated spectral variations between segments are assigned a 1% uncertainty to match segment-to-segment differences observed in Monte Carlo simulations of the Phase I AD-I. A simulation-predicted background shape is used (see Fig. 20), and the signal-to-background ratio adjusted to account for the  $1/r^2$  flux reduction at farther positions.

The sensitivity of PROSPECT to  $\bar{\nu}_e$  oscillation after 1 and 3 calendar years (6 and 18 reactor cycles, respectively) is shown in Fig. 8. In the first year of data taking, AD-I will be operated equally at two positions separated by  $\sim 1.5$  m. The 3-year run will further increase baseline coverage with deployment at a third location separated by an additional  $\sim 1.5$  m from the front position. Within a single calendar year, PROSPECT can probe the best-fit of all current global analyses of  $\nu_e$  and  $\bar{\nu}_e$  disappearance [4, 5] at  $4\sigma$  confidence level. Over 3 years of operation, PROSPECT Phase I can discover oscillations as a sign of sterile neutrinos at  $>3\sigma$  over the majority of suggested parameter space. The sensitivity

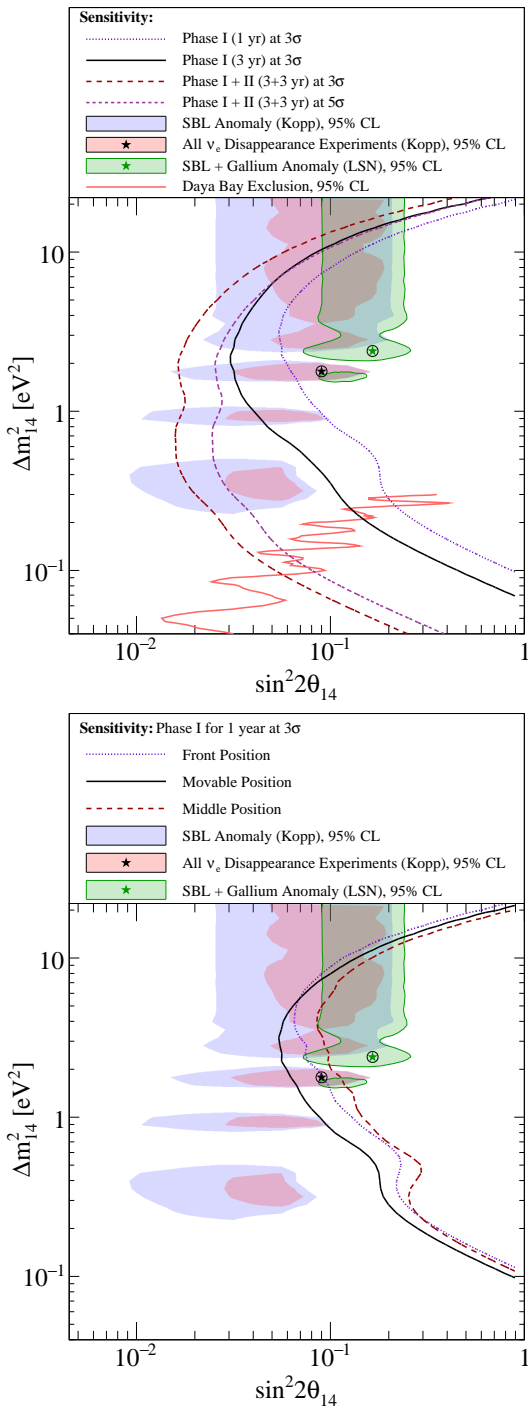


FIG. 8. (Top) PROSPECT Phase I and Phase II sensitivities to a single sterile neutrino flavor. Phase I probes the best-fit point at  $4\sigma$  after 1 year of data taking and has  $>3\sigma$  reach of the favored parameter space after 3 years. The combined reach of Phase I+II after 3+3 years of data taking yields a  $5\sigma$  coverage over the majority of the parameter space below  $\Delta m_{14}^2 \sim 10 \text{ eV}^2$ . Daya Bay exclusion curve is from [57]. (Bottom) Increase in oscillation sensitivity to sterile neutrinos during Phase I by operating AD-I at two positions instead of at the front or middle position only.

Parameter	Value
<b>Reactor</b>	
Power	85 MW
Shape	Cylinder
Size	0.2 m $r \times$ 0.5 m $h$
Fuel	HEU
Duty cycle	41% reactor-on
<b>Antineutrino Detector 1 (AD-I)</b>	
Cross-section	$1.2 \times 1.45 \text{ m}^2$
Proton density	$5.5 \times 10^{28} \text{ p/m}^3$
Total Target Mass	2940 kg
Fiducialized Target Mass	1480 kg
Baseline range	4.4 m
Efficiency in Fiducial Volume	42%
Position resolution	15 cm
Energy resolution	$4.5\%/\sqrt{E}$
S:B Ratio	3.1, 2.6, 1.8
Closest distance	6.9 m, 8.1 m, 9.4 m
<b>Antineutrino Detector 2 (AD-II)</b>	
Total Target Mass	$\sim 10 \text{ ton}$
Fiducialized Target Mass	$\sim 70\%$
Baseline range	$\sim 4 \text{ m}$
Efficiency in Fiducial Volume	42%
Position resolution	15 cm
Energy resolution	$4.5\%/\sqrt{E}$
S:B ratio	3.0
Closest distance	15 m
<b>Operational Exposure</b>	
Phase I	1, 3 years
Phase II	3 years

TABLE I. Nominal PROSPECT experimental parameters. Phase I consists of operating AD-I for three years split between front, middle, and back positions. Phase II adds AD-II at a longer baseline and operates both detectors for three additional years.

achieved with Phase II is also shown: after 3 additional years of operation essentially all parameter space suggested by  $\nu_e$  disappearance data below  $10 \text{ eV}^2$  can be excluded.

The dependence of the sensitivity on experimental parameters is examined in Table II. These results clearly validate the design focus on background rejection and maximizing target mass, while also highlighting the value of covering the widest possible baseline range via movement of AD-I. The increase in sensitivity afforded by the expanded  $L/E$  coverage gained through AD-I movement is further illustrated in the bottom panel of Fig. 8. Although the signal decreases as the inverse of  $r^2$ , the gain from  $L/E$  coverage surpasses the loss due to reduced signal when the detector is operated equally at two positions. It must be noted that for the sensitivity calculation shown this gain is purely from the improved  $L/E$  coverage. Moving the detector also gives a better control of correlated and uncorrelated systematic biases, which can be expected to further increase the sensitivity. The ultimate choice of positions will be guided by the demonstrated S:B at various baselines.

	Decreased	Nominal	Increased
<b>Position</b>	<i>Front only</i>	<i>Movable</i>	<i>Middle only</i>
	2.79	4.60	2.37
<b>Position</b>	<i>10cm</i>	<i>14.6cm</i>	<i>20cm</i>
<b>Resolution</b>	4.69	4.60	4.46
<b>Efficiency</b>	32%	42%	52%
	3.84	4.60	5.26
<b>Energy</b>	3%	4.5%	20%
<b>Resolution</b>	4.61	4.60	4.20
<b>Background</b>	$\times 0.33$	–	$\times 3$
<b>Suppression</b>	3.92	4.60	5.00
<b>Bin-to-Bin</b>	0.5%	1.0%	2.0%
<b>Uncertainty</b>	4.69	4.60	4.30
<b>Relative Segment</b>	0.5%	1.0%	2.0%
<b>Normalization</b>	4.60	4.60	4.59
<b>Detector</b>	$10 \times 8$	$12 \times 10$	$14 \times 12$
<b>Size</b>	3.23	4.60	6.02

TABLE II. The effect of varying experimental parameters (*italic*) on the confidence level in the unit of  $\sigma$  with which oscillations at the Kopp best-fit point can be differentiated from the null hypothesis with one year of data-taking.

### B. Precision Measurement of the Reactor $\bar{\nu}_e$ Spectrum

PROSPECT will measure the energy spectrum of  $\bar{\nu}_e$  emitted by an HEU reactor with a precision that exceeds previous experiments and current model predictions. Between 2–6 MeV, Phase I will achieve an average statistical precision better than 1.5% and systematic precision better than 2%. The target energy resolution,  $4.5\%/\sqrt{E}$ , will be greater than any previous reactor experiment and will allow for the detection of fine structure in the antineutrino spectrum. In contrast to LEU reactors where the fission fractions change as plutonium isotopes are produced in the core, the simpler HEU system allows for a more accurate evaluation of reactor evolution and flux prediction models.

Fig. 9 shows the differences between three current models: two based on the  $\beta^-$ -conversion method, and one based on *ab-initio* calculation. To highlight the shape differences between models, they are shown in ratio to a smooth approximation  $F(E)$ [60]. The PROSPECT Phase I statistical precision is shown as the black error bars. PROSPECT will be able to discriminate between these models and directly measure the spectrum more precisely than any of the predictions. In addition, this measurement can be combined with those underway at LEU reactors to extract the non- $^{235}\text{U}$  contribution to the spectrum. Since current LEU measurements, and that of HEU which we propose, are expected to have percent-level precision, differences should be prominent and provide another route to evaluate and refine reactor models.

The segmented AD-I detector is designed to enhance the spectral measurement through careful optimization of detector uniformity and construction techniques. The use of low-mass reflector panels, described in more

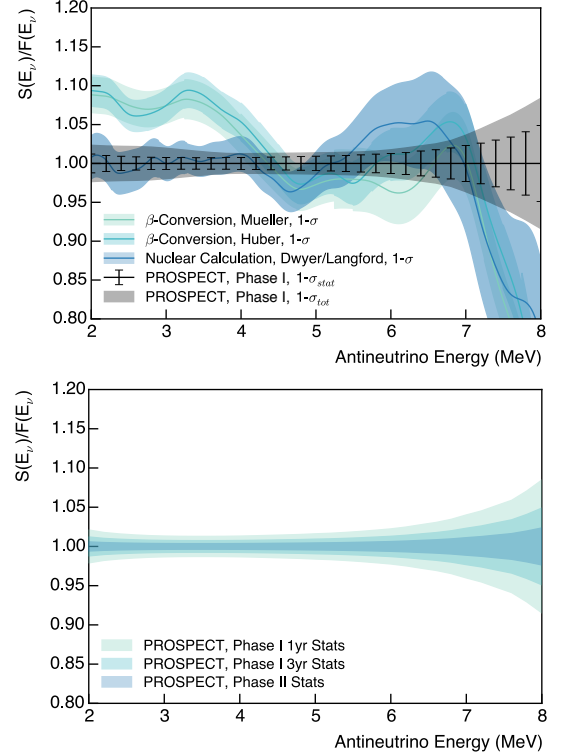


FIG. 9. (Top) Three models of the  $^{235}\text{U}$   $\bar{\nu}_e$  energy spectrum relative to a smooth approximation. The  $1\sigma$  error band of the Phase I measurement including subtraction of predicted background (error bars) and systematic uncertainties (gray band) are shown for comparison. An energy resolution of  $4.5\%/\sqrt{E}$  has been applied to highlight accessible features. (Bottom) Evolution of statistical error bands for 200 keV bins from Phase I to Phase II.

detail in Sec. V A, minimizes the non-scintillating volume that could bias the detected energy spectrum. Multiple fiducialization schemes are being studied to determine the optimum volume selection that maximizes detection efficiency of positron annihilation gammas.

AD-II is designed to achieve at least equal statistical power to that of AD-I, even at a longer baseline. A larger target mass and improved cosmogenic shielding increase the IBD detection rate without decreased signal-to-background ratio. Both antineutrino detectors AD-I and AD-II are comprised of identical segments, ensuring that systematic uncertainties will be consistent. Thus, all development and characterization of AD-I will directly apply to AD-II, simplifying the combined analysis during Phase II.

Fig. 9 shows a comparison of the statistical error bands, assuming 200 keV binning, for each experimental phase. With Phase II, PROSPECT will achieve an average of 1.0% statistical uncertainty throughout the reactor antineutrino energy range. With the combined phases, PROSPECT will have major statistical power to resolve and probe the spectral anomaly region and di-

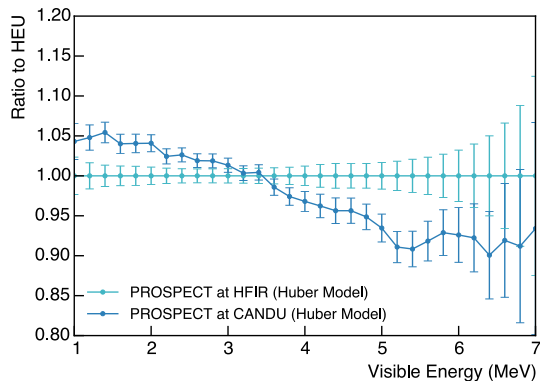


FIG. 10. Ratio of 3 year simulated measurements at HFIR and a CANDU reactor, assuming identical statistics and backgrounds. Only statistical uncertainties are shown, as systematics will cancel. This *time independent* difference in spectra is due to differing fuel mixes.

rectly measure fine structure in the antineutrino spectrum.

### C. Reactor Monitoring and Characterization

Phase I of the PROSPECT experiment will develop technology, produce scientific results, and construct a detector that could find utility in other areas.

While the highest priority for future spectrum measurements are HEU-fueled reactors, examination of other reactor types is also valuable. Measurement of a LEU reactor spectrum with the superior energy resolution of the PROSPECT AD-I would supplement current statistically precise measurements [6–8], improve the knowledge of  $\bar{\nu}_e$  spectra from fission of  $^{238}\text{U}$ ,  $^{239}\text{Pu}$  and  $^{241}\text{Pu}$ , and reduce systematic uncertainties in the comparison of LEU and HEU  $\bar{\nu}_e$  spectra through use of a common detector for both measurements. Measurement of a CANDU reactor [61, 62], in which frequent refueling maintains a static fuel mixture of  $^{235}\text{U}$ ,  $^{238}\text{U}$ ,  $^{239}\text{Pu}$ , and  $^{241}\text{Pu}$ , would further improve the determination of each spectral component. Reactors with different core neutron spectra, which populate different fission daughter distributions, should also be considered. PROSPECT has contacts at several candidate reactors for such follow-up measurements after its run at HFIR.

Compact  $\bar{\nu}_e$  detector development is also of interest for reactor monitoring applications [63–65]. PROSPECT will advance these efforts through development of background rejection techniques, demonstration of near-surface  $\bar{\nu}_e$  detection, and precision  $\bar{\nu}_e$  spectrum measurement in compact detectors. These capabilities are of interest to potential end users of reactor monitoring technology [66, 67]. Successful demonstration of reactor  $\bar{\nu}_e$  flux and spectrum measurements near-surface would open a range of possibilities for deployment at

various baselines that would otherwise be inaccessible.

## IV. PROSPECT Experimental Strategy

PROSPECT is conceived as a phased experiment involving two independent detectors at multiple baselines. Phase I consists of a movable antineutrino detector, AD-I, with a 3-ton active target mass at baselines ranging from 7–12m from the reactor core. Phase II of the experiment involves an additional second detector, AD-II, of  $\sim 10$ -tons deployed at 15–19 m from the core. High-impact first physics results can be produced after 1 year of data taking in Phase I. The physics goals of Phase I can be completed with 3 years of data taking of AD-I. The ultimate physics reach of PROSPECT is obtained after an additional 3 years of simultaneous operation of AD-I and AD-II.

### A. Reactor Site

After a thorough study of three possible US research reactor sites, all of which could support the experimental goals, HFIR at ORNL was selected for Phase I of PROSPECT. Facility parameters, including the size and power of the compact HEU fueled core, and operational duty cycle are given in Table I. Deployment locations for both AD-I and AD-II, shown in Fig. 3, have excellent access and controllable reactor-correlated and cosmogenic background levels. Through extensive engagement with HFIR, it has been established that AD-I and the associated passive shielding design meets all space, floor-loading, and safety requirements and would permit a  $\sim 3$  m range of horizontal movement.

Extensive background measurements at AD-I locations have identified specific “hot spots” that can be reduced with localized shielding (Sec. IV D 1). There is no significant reactor-correlated background at the AD-II location. Prototype detector and shielding tests show that reactor-produced  $\gamma$ -ray and neutron backgrounds can be suppressed to insignificant levels with appropriate shielding (Sec. IV D 4). Remaining time-correlated backgrounds are dominated by cosmogenic fast neutrons since the detector sites have minimal overburden. Shielding for AD-I will therefore have fixed lead walls to control reactor backgrounds and shielding that moves with the detector to reduce cosmogenic backgrounds.

### B. Antineutrino Detector Design and Performance

The PROSPECT antineutrino detector (AD-I) for Phase-I consists of a single volume of  $^6\text{Li}$ -loaded liquid scintillator (LiLS) segmented by low-mass high-reflectivity optical separators. The AD-I detects reactor  $\bar{\nu}_e$  via the inverse beta decay (IBD) reaction  $\bar{\nu}_e + p \rightarrow$

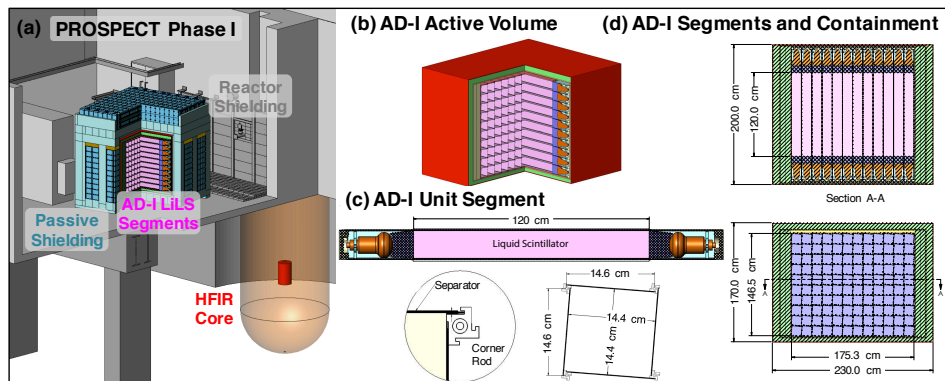


FIG. 11. (a) Model of AD-I for Phase I at HFIR. (b) A cutaway diagram of the AD-I. (c) The unit segment structure. (d) Inner and outer dimensions of the AD-I.

$e^+ + n$ . The positron carries most of the  $\bar{\nu}_e$  energy and makes a prompt energy signal in the LS. The neutron thermalizes before capture on  ${}^6\text{Li}$  or hydrogen, producing a delayed signal  $\sim 40 \mu\text{s}$  later.  ${}^6\text{Li}$  doping was chosen as its decay products produce easily recognized, localized energy depositions in pulse shape discrimination-capable LS. This time-correlated signature of a gamma-like prompt signal and a neutron-capture-like delayed signal is extremely effective at nearly eliminating randomly time-coincident (accidental) backgrounds.

The optical separators divide the total active volume ( $\sim 3000$  l) into 120 individual segments (Fig. 11) providing baseline and event topology information independent of light transport and timing. Each segment shares optical separator panels and hollow support rods with its nearest neighbors and is read out at both ends by photomultiplier tubes (PMTs). Space constraints have largely determined the designed segment length, while cross-section dimensions are constrained by the physical dimensions of the PMTs and their housing assemblies. To maintain LiLS compatibility, the PMT and its voltage divider are housed inside a polycarbonate module with a light guide for optical coupling. Modules are bolted together (10 high  $\times$  12 long) to form a support structure for the optical separator array. The separator panels and corner rods are designed to minimize inactive material and amount to 1.8% of the total target mass. This is significantly less than earlier experiments such as Bugey 3 (15.5% inactive mass) [68]. A carefully selected subset of the support rods house either optical fibers or tubes containing movable radioactive sources to calibrate segment energy response and timing. Cables, fibers, and calibration tubes are routed to the top surface, and this inner detector structure is inserted into a sealed acrylic single-volume LiLS containment vessel that isolates the inner detector from outside moisture and oxygen. All space between PMT modules is filled with LiLS. The inactive LiLS not viewed by PMTs acts as additional passive shielding and totals  $\sim 300$  l.

The PROSPECT LiLS has been developed over several

years to exhibit the light yield and pulse shape discrimination (PSD) required for the experiments physics (energy resolution) and background rejection (PSD) goals (Sec. IV D 2). Enriched  ${}^6\text{Li}$ , fluors (PPO) and wavelength shifter (bis-MSB) are added to a commercial scintillator base (EJ-309, Eljen Technologies [69]). Prototype studies in a 20 l, 1 m-long, test detector have demonstrated that a detected light yield of 6500 photons per MeV and a bulk attenuation length of 4 m are achievable, leading to an energy resolution of better than  $4.5\%/\sqrt{E}$ . The excellent PSD performance demonstrated in Sec. IV D 3 enables cuts preserving 99.9% of the (n,Li) signal while rejecting the same fraction of  $\gamma$ -ray events.

Detailed simulations based on measured backgrounds at HFIR and performance of prototypes indicate that PROSPECT can achieve and exceed the required signal-to-background performance of 1:1 (Fig. 20). Further details are given in Sec. V.

For Phase II, a second antineutrino detector, AD-II, would be installed just outside the HFIR reactor building covering baselines from 15–19 m. The detector features an increased volume of  $\mathcal{O}(10)$  tons, while maintaining the same segmentation as AD-I. By using identical segment geometries, systematic uncertainties related to relative detector efficiency can be better controlled and confidence in the projected background rejection is increased. The active detector would be shielded by  $\sim 0.75$  m of steel and 1 meter of polyethylene or water (nearly 5 m of water equivalent mass) to reduce cosmogenic backgrounds. Simulations predict a signal-to-background ratio of about 3.0, comparable to the closest AD-I position from the reactor core.

### C. Calibration Strategy

The segmented AD-I design incorporating hollow support rods will allow extensive access to the full AD-I volume for routine calibration using optical fibers or retractable radioactive sources (Fig. 12). LiLS light transmission, PMT gain, and PMT timing will be calibrated

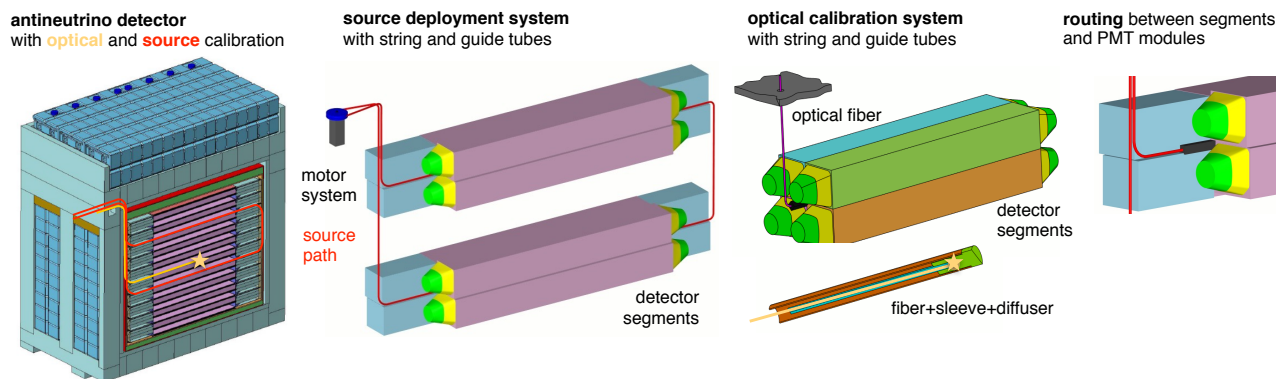


FIG. 12. The AD-I source deployment and optical calibration systems. Radioactive sources and an optical system will be deployed between detector segments.

and monitored with a stabilized pulsed laser source via optical fibers, with each fiber illuminating 4 segments at their midpoint. Encapsulated  $\gamma$ -ray and neutron sources on tensioned string loops will be periodically deployed at multiple locations within the AD-I via Teflon guide tubes in the support rods.

Fitting the deposited energy spectra of radioactive sources will allow the absolute positron energy scale, including scintillator non-linearity, to be calibrated to a few percent or better. These sources can also be used to ensure that small expected differences in positron energy scale between fiducial segments can be characterized to the percent level and corrected for in PROSPECT's sterile oscillation analysis. Neutrons from encapsulated AmBe sources will allow calibration of PSD and determination of neutron detection efficiencies in each segment. Radioactive and cosmogenic backgrounds will be used to monitor and calibrate the detector response between source deployments, following the example of PROSPECT-20 which used  $^{40}\text{K}$ , neutron capture on  $^6\text{Li}$ , and through-going muons. Finally, the possibility of spiking the scintillator with  $\mathcal{O}(10^{-13} \text{ g})$  of  $^{227}\text{Ac}$  to exploit the double- $\alpha$  cascade from  $^{219}\text{Rn} \rightarrow ^{215}\text{Po} \rightarrow ^{211}\text{Pb}$  is being examined. This will allow a measurement of the uniformity per segment to 1% and enable a relative LiLS mass measurement. Further R&D is needed to ensure that dissolution and uniform distribution is possible without introducing unwanted backgrounds.

#### D. Research and Development Status

The PROSPECT collaboration has conducted a vigorous R&D program since 2013 [59] and is exceptionally well prepared to perform the physics measurements described in Sec. III. Here we describe the central elements of that R&D program including logistics and background studies at multiple reactors, detector design, liquid scintillator development, prototype opera-

tion, and simulation development and validation. Collectively, these efforts demonstrate that the PROSPECT AD-I design for Phase I can be installed in a research reactor facility, meet the necessary performance requirements, and that both reactor-generated and cosmogenic backgrounds can be controlled.

##### 1. Reactor Facility Background Measurements

To obtain the broadest sensitivity to the possible existence of additional neutrino states [58] and to maximize the event rate for a precision  $\bar{\nu}_e$  energy spectrum measurement, Phase I PROSPECT must be placed as close to a reactor core as is practical. In such a location,  $\gamma$ -rays and neutrons produced by reactor operation cannot be neglected, and indeed would be the dominant background source without careful attention to shielding. Furthermore, most facilities have minimal overburden, thus cosmogenic backgrounds are significant relative to the expected signal rate. In particular, fast neutrons from air showers can yield backgrounds that are challenging to shield, either with passive or active approaches.

The PROSPECT collaboration has conducted a careful assessment of natural and reactor generated background radiation that is reported in [54]. These measurements included high and moderate resolution  $\gamma$ -ray spectroscopy, fast and thermal neutron flux, muon flux, and fast neutron spectroscopy. Reactor facilities exhibit significant spatial variation in both  $\gamma$ -ray and neutron backgrounds due to irregular shielding, localized shielding leakage paths, or piping carrying activated materials (Fig. 13), thus site-specific characterization of background is essential to optimize a shielding design. Localized shielding applied to compact background sources can be a cost- and weight-efficient approach to reducing background. Such an approach has been demonstrated quite successfully at the HFIR site (Fig. 13). The measurements described in Section IV D 4 show that targeted shielding, in addition to a carefully

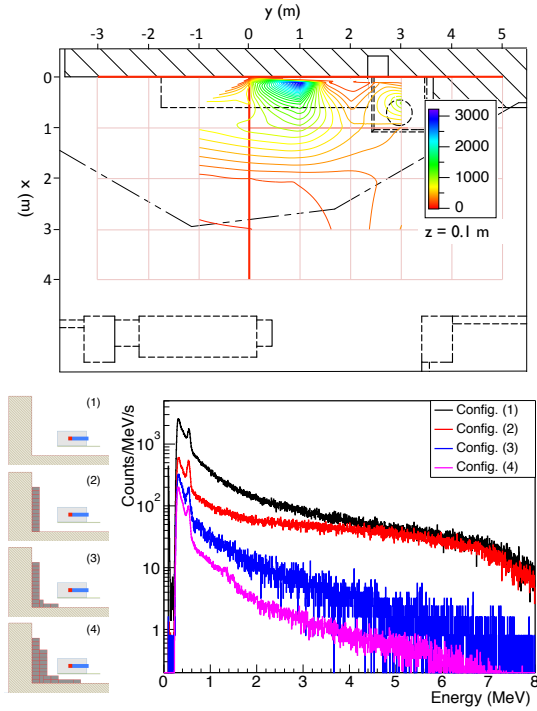


FIG. 13. (Top)  $\gamma$ -ray count rates ( $s^{-1}$ ) for an unshielded 2" NaI(Tl) detector with HFIR at power. The core is at  $(x, y, z) = (-4.06, 0, -3.85)$ . Strong spatial variation is caused by a plugged beam tube located at  $(x, y, z) = (0, 1, 0)$ . (Bottom) Energy spectra for a horizontally collimated 2" NaI(Tl) detector for varying configurations of a lead wall, with HFIR at power. The shield is centered at the location of highest  $\gamma$ -ray intensity,  $(x, y, z) = (0, 1, 0)$ . The background rate is significantly reduced, even at high energies.

designed shielding package, can yield excellent control of reactor related backgrounds.

The flux and spectrum of cosmogenic fast neutrons observed within the minimal overburden provided by the HFIR building is essentially unaltered compared to standard reference measurements (e.g. [70, 71]), which can therefore be used as source terms in simulation studies. The results of these studies have been integral to the design of the Phase I PROSPECT AD-I and have been validated using a series of prototype detectors as described in Section IV D 3. The detailed understanding of fast neutron related backgrounds afforded by this work has enabled the development of a series of effective analysis cuts that yield an expected S:B of better than 1:1 as described in Section V.

## 2. Liquid Scintillator Development

Liquid scintillator is the standard detection medium for reactor  $\bar{\nu}_e$  detectors due to the high abundance of free proton targets, providing excellent pulse shape discrimination, high light yield, and lower cost than plastic scintillator. Liquid scintillators are frequently

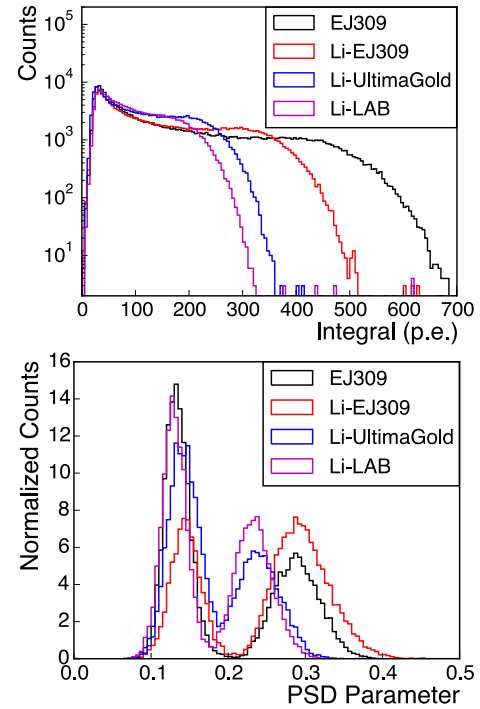


FIG. 14. Comparison between unloaded EJ-309 and three different LiLS formulations. (Top) Response to  $^{60}\text{Co}$ , demonstrating the relative light yield. (Bottom) Comparison of PSD distributions when exposed to  $^{252}\text{Cf}$ . Li-EJ309 has the best performance amongst Li-loaded materials.

loaded with gadolinium to decrease the mean neutron capture time and yield a high-energy capture signal. However, gadolinium is ill-suited to compact detectors where neutron-capture  $\gamma$ -rays will often escape the active volume. Neutron capture on  $^6\text{Li}$  produces a highly localized ( $\ll 1$  mm) energy deposition from the reaction  $n + ^6\text{Li} \rightarrow \alpha + t + 4.78$  MeV, making it well suited for use in compact detectors. While the high  $dE/dx$  of the alpha and triton results in a quenched light yield (electron equivalent energy of  $0.6$  MeV $_{ee}$ ), it also allows discrimination from equivalent-energy electromagnetic backgrounds using the PSD capability of certain liquid scintillators.

Previously available Li-loaded liquid scintillators were based on toxic and flammable solvents that can no longer be used in reactor facilities. Therefore, a multiyear research and development effort has explored the feasibility of three new low-toxicity and high-flashpoint scintillator bases, LAB, UltimaGold, and EJ-309 [69, 72]. Surfactants are used to form a micro-emulsion containing  $^6\text{LiCl}$ , creating a dynamically-stable mixture that retains the PSD capability of the base scintillator. Extensive studies were performed with each formulation to characterize light yield and PSD performance using  $\gamma$ -ray and neutron sources.

The EJ-309-based LiLS was found to have the best light yield and PSD performance (Fig. 14). Li-EJ309 has

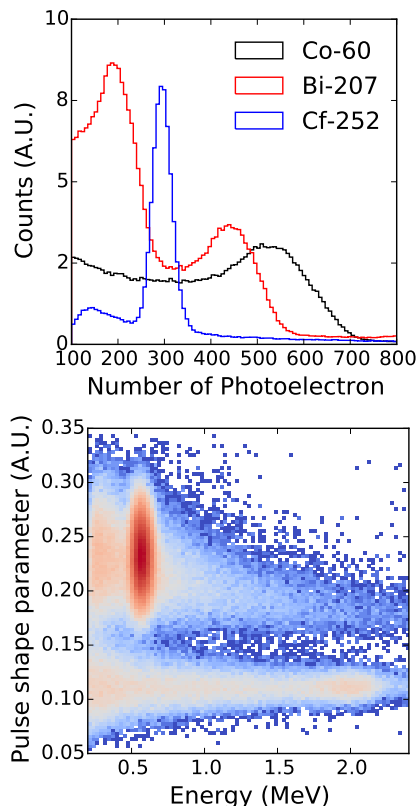


FIG. 15. (Top) Measured PE spectra including the Compton edge of  $^{60}\text{Co}$  and  $^{217}\text{Bi}$   $\gamma$ -rays and the quenched  $(n, \text{Li})$  capture peak from  $^{252}\text{Cf}$  neutron source. (Bottom) PSD performance of Li-EJ309. The upper band is neutron-like events with  $(n, \text{Li})$  captures at  $\approx 0.6$  MeV dominating the statistics. The lower band shows  $\gamma$ -like events.

a proton density of  $5.5 \times 10^{22}/\text{cm}^3$ , light yield above 6500 photons/MeV, and a bulk attenuation length of  $\sim 4$  m. The stability of Li-EJ309 samples has been monitored for approximately one year, with the light yield shown to be stable within the 2% measurement uncertainty.

A materials compatibility program studied all components potentially in contact with Li-EJ309 for extended periods of time. The AD-I interior will be constructed only with components that have been qualified, i.e. found to be stable and not degrade LS performance. Acceptable materials include cast acrylic, Teflon, polycarbonate and PLA plastics (clear and colored), Viton, and Acetal.

### 3. Detector Prototyping

PROSPECT has prototyped many key elements of the proposed AD-I design, including constructing test detectors to validate the light collection efficiency and PSD performance and the low-mass reflector system that optically segments the active liquid scintillator target.

An acrylic test detector ( $15 \text{ cm} \times 15 \text{ cm} \times 1 \text{ m}$ ), referred to as "PROSPECT-20", was produced to validate the performance of the AD-I optical design. The effects of different PMT models, single versus double-ended readout, reflector types and coupling methods have been explored and reported in [73]. As shown in Fig. 16, the detector utilized internal reflectors similar to the low-mass panels discussed below and the R6594 PMTs chosen for AD-I [74]. Filled with EJ-309 [69], a light collection of  $841 \pm 17$  photoelectrons (PE)/MeV was observed with excellent PSD performance: a rejection factor of  $10^4$  for  $\gamma$ -rays was achieved while preserving 99.9% of the  $(n, \text{Li})$  capture signal between 0.5–0.7 MeV. In addition, both PSD and light collection were found to be totally uniform along the length of the cell within systematic and statistical uncertainties. Position reconstruction along the long axis of PROSPECT-20 utilizing light arrival time differences between PMTs was also demonstrated with a 5 cm resolution.

When filled with LiLS an average light collection of  $522 \pm 16$  PE/MeV was measured with three  $\gamma$ -ray sources in the range 0.38–2.0 MeV (Fig. 15). The demonstrated PE/MeV exceeds the goal of 500 PE/MeV needed to achieve the target  $4.5\%/\sqrt{E(\text{MeV})}$  energy resolution. Excellent uniformity and PSD performance was again demonstrated at the  $(n, \text{Li})$  capture peak and above (Fig. 15) enabling preservation of 99.9% of the  $(n, \text{Li})$  signal while rejecting the same fraction of  $\gamma$ -ray events. The mean neutron capture time is observed to be 40  $\mu\text{s}$ .

For the optical segmentation system, low-mass reflector panels have been developed by adhering 3M Enhanced Specular Reflector (ESR) [75] to both sides of a rigid 0.6 mm thick carbon fiber sheet, and then enclosing this assembly in a Teflon sleeve via heat bonding. The result is a large area, low-mass, highly reflective assembly that is hermetic and liquid scintillator-compatible. A structural support system, described in Sec. IV B, was prototyped using polycarbonate and 3D-printed white PLA plastic, which allowed for rapid fabrication and testing cycles. A nine-segment mechanical mock-up of the structure has been used to develop assembly procedures and demonstrate the mechanical robustness of the segmentation system.

### 4. Onsite Prototype Detector Operation and Simulation Validation

PROSPECT has deployed multiple liquid scintillator prototype detectors and shielding packages at HFIR since mid-2014 to characterize backgrounds *in-situ* and develop a working knowledge of facility regulations, operating procedures and work control processes. Detector size was increased by a hundredfold, from an initial 100 ml EJ-309 cell to a 23 l cell containing LiLS (PROSPECT-20). The shielding packages have likewise grown from a small lead brick cave to a multilayered

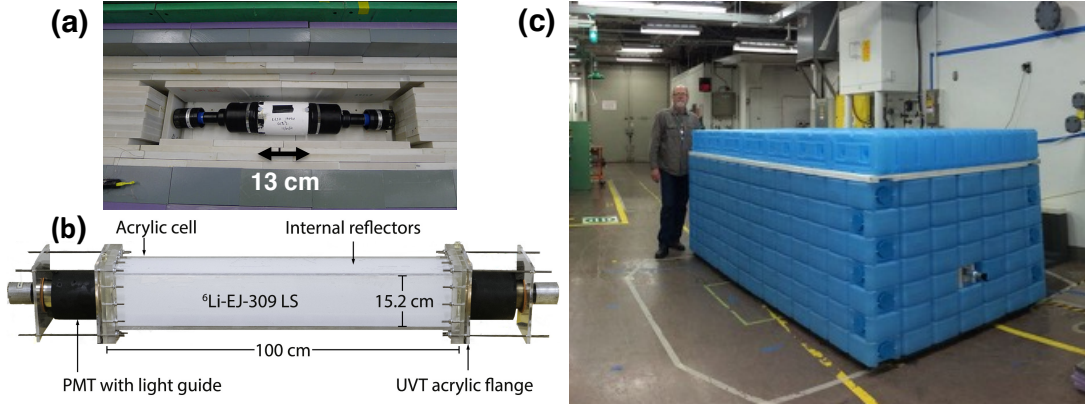


FIG. 16. Prototype detectors and shielding installed at the HFIR experimental location. (a) The PROSPECT-2 prototype within a partially assembled polyethylene and lead shield. (b) The PROSPECT-20 prototype with internal reflectors added after operation at HFIR. (c) The PROSPECT-20 shielding enclosure at HFIR.

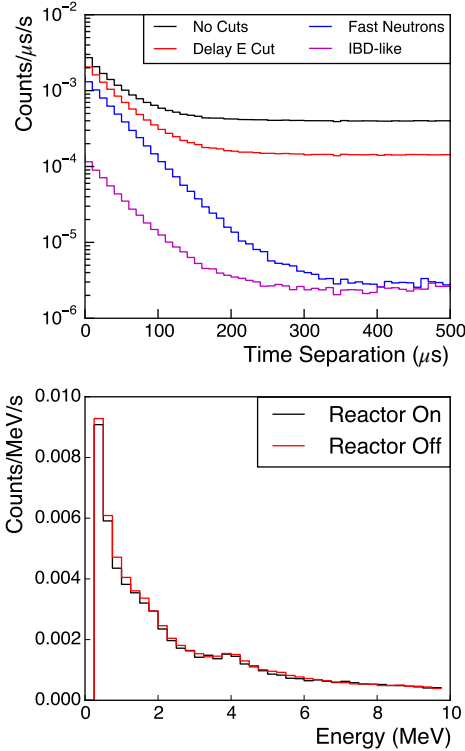


FIG. 17. (Top) Time separation between prompt and delayed signals (black) for reactor-off operation of PROSPECT-20 with different analysis cuts applied: delay energy (red), fast neutrons (blue), and IBD-like (purple). (Bottom) Comparison of PROSPECT-20 IBD-like event prompt energy spectra with HFIR on (black) and off (red).

shield of water bricks [76], High Density Polyethylene (HDPE), 5% borated HDPE and lead with a total volume nearly 1/4 that of the proposed AD-I design (Fig. 16).

Data have been collected over nine months through multiple reactor cycles. Analysis cuts were developed

to isolate IBD-like events and elucidate the event types that produce background at this location. The time separation (Fig. 17 top) spectrum between prompt and delayed signals is dominated by a random background that is constant in time, but also exhibits an exponentially decaying time-correlated component consistent with that observed for correlated particle processes that terminate in a neutron capture. IBD is one such process (prompt  $e^+$  followed by neutron capture), as are correlated backgrounds due to fast neutron recoil followed by capture or capture of multiple spallation neutrons.

Application of a simple energy cut around the  $(n,\text{Li})$  capture peak for the delayed signal in an event pair reduces the random component by a factor of 2.8, demonstrating, in part, the utility of LiLS for a compact detector. Applying selections based upon PSD provides further information: requiring that the prompt signal fall in the neutron recoil band (blue curve in Fig 17) indicates that the majority of time-correlated background events in PROSPECT-20 are due to fast neutron recoil followed by capture. Finally, applying selections consistent with IBD events (prompt PSD in  $\gamma$ -like band, delayed signal in  $(n,\text{Li})$  energy and PSD region) reduces the initial coincidence rate by a factor of 55 and reveals the IBD-like background to be dominated by time-correlated pairs (magenta curve). Accidental coincidences due to reactor-produced  $\gamma$ -rays following this selection are minimal due to the selectivity of the  ${}^6\text{Li}$  neutron capture signature and targeted shielding applied to background “hot-spots” at HFIR. Comparison of IBD-like event energy spectra with the reactor on and off (Fig. 17 bottom) indicates that IBD-like backgrounds are cosmogenic and that reactor generated backgrounds are negligible.

## E. Timeline

PROSPECT Phase I will be ready to proceed in early 2016. Design, construction, assembly, and installation of AD-I will take approximately one year. Installation of components in the HFIR experimental room is restricted to the reactor-on periods due to limited availability of HFIR craft labor during reactor shutdowns and maintenance periods. Detector assembly and installation will be completed by the end of calendar year 2016. After a brief period of commissioning, data taking will start in early 2017. AD-I will run continuously for three years over all reactor-on/off cycles. Periodic calibrations are planned and will minimally interrupt continuous data taking. At least three detector movements to different baselines are planned. Since AD-I and the associated shielding are mounted on air bearings, no disassembly is required. Detector repositioning and restart will take  $\leq 2$  days and will have minimal impact on data collection. With timely funding, construction of Phase II could start soon, with data taking about 2–3 years later.

## V. Predicted Detector Response: Signal and Background

A comprehensive and flexible Monte Carlo simulation of the PROSPECT detector design has been developed using the GEANT4 package [77]. Particle interactions are based on the “QGSP\_BERT\_HP” physics list in GEANT4.10.01p1, which focuses on “high precision” models for lower-energy neutron interactions. Optical photon generation and tracking is optionally available for light transport modeling. The simulation includes geometries for prototype test detectors and the two ADs. A variety of event generators are available, including inverse beta decay, CRYv1.7 [78] for cosmic ray shower generation, a parametrized model for the surface cosmic neutron spectrum [79], and calibration sources.

### A. Response to the Reactor $\bar{\nu}_e$ Signal

Simulation studies have been used to study the response of the PROSPECT AD-I design to the inverse beta decay signal and many classes of background events. This includes particle transport studies using GEANT4 and examination of segment optical response using both GEANT4 and the SLitrani package [80]. Exploratory studies of segment response confirmed that the choice of an efficient specular reflector, with a component of total internal reflection (TIR) from the Teflon layer encapsulating the segment wall, provided good collection efficiency and uniformity along the entire segment volume. Good agreement was found with the data from the PROSPECT-20 (P20) detector using various reflector and light guide configurations.

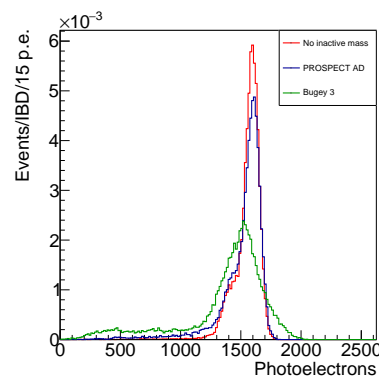


FIG. 18. Simulated response to 4 MeV  $e^+$  for AD-I configurations with no inactive mass (red), the PROSPECT low mass optical separators (blue), and an inactive mass fraction equivalent to Bugey 3 (green).

The response to the  $e^+$  produced by IBD is of particular interest and has been examined for a wide range of segment size, segment wall compositions, and optical configurations. The  $e^+$  response achieved with the AD-I design described above is illustrated in Fig. 18, which includes both particle and optical scintillation photon transport. Here, the response to mono-energetic 4 MeV positrons distributed uniformly throughout the fiducial detector volume is examined for several segment wall configurations: walls with infinitesimal thickness (no inactive mass in active volume), the AD-I design, and a thickness equivalent to that used in the segmented Bugey 3  $\bar{\nu}_e$  detector [81]. The AD-I configuration of low-mass separators has comparable performance to a detector without inactive material and is significantly better than the segmented Bugey 3 detector.

### B. Backgrounds from Cosmogenic Activity

Data collected using the PROSPECT-20 detector at HFIR have been used to validate the PROSPECT AD-I simulation. For example, Fig. 19 displays an absolute comparison between data and simulation of cosmic ray shower backgrounds. Both the energy and time distributions of IBD-like events are in good agreement, with the results being consistent with fully explaining the observed IBD-like rate in PROSPECT-20. Although the IBD-like background rate is higher than the expected  $\bar{\nu}_e$  interaction rate, improved shielding and cuts possible in the full AD-I will suppress backgrounds substantially, achieving a signal-to-background ratio of  $\geq 1$  according to simulation.

The validated simulation package indicates that measured IBD-like background in PROSPECT-20 is primarily due to high-energy (tens to hundreds of MeV) cosmic neutrons, with small additions from muon interactions and accidental  $\gamma$ -ray coincidences. These mechanisms are also projected to be the primary source of

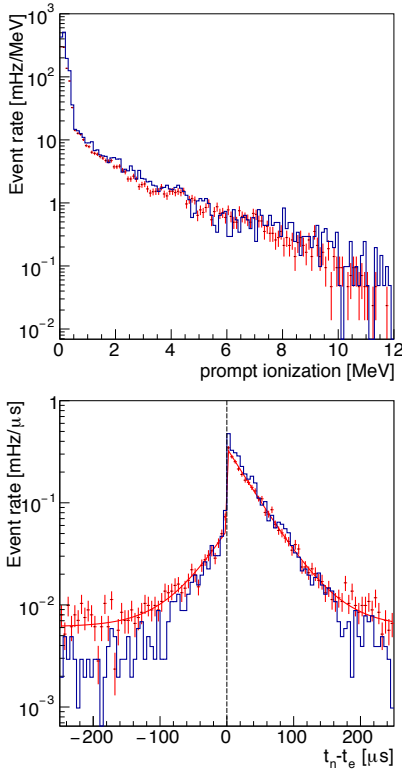


FIG. 19. (Top) PROSPECT-20 IBD-like energy distributions from reactor-off data (red) compared to simulation for cosmic backgrounds (blue). (Bottom) PROSPECT-20 IBD-like timing distributions from reactor-off data (red) compared to simulation for cosmic backgrounds (blue).

IBD-like background events in the PROSPECT AD-I. By design, the multi-segment AD-I provides information useful for identifying and vetoing most cosmic background events. However, high-energy cosmic neutrons, which can penetrate undetected deeply into the active volume before inelastic scattering interactions, can produce time-correlated prompt ionization, highly quenched nuclear recoils, and delayed secondary neutron capture signals, and are projected to be the main background source. The rates of cosmogenically-produced  ${}^9\text{Li}$  and  ${}^8\text{He}$ , which also mimic IBD signals, are estimated to be roughly two orders of magnitude below the IBD rate, and can be measured with reactor-off data.

After identification of candidate prompt and delayed signals via deposited energy and PSD selections, additional cuts on event topology (including both time and position information) provide two to three orders of magnitude in background suppression. Fig. 20 demonstrates the effectiveness of topology cuts at rejecting cosmic ray background relative to the IBD signal.

The event selections are as follows. “Time topology” cuts include: (1) delayed capture must occur within  $100\ \mu\text{s}$  of the prompt ionization; (2) multiple hits in the prompt cluster must occur within  $5\ \text{ns}$  to reject slower-moving neutron recoil events; (3) events

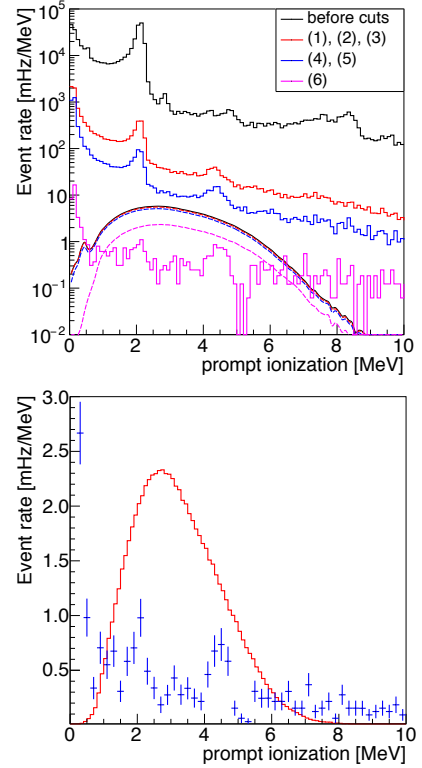


FIG. 20. (Top) Simulated AD-I IBD signal and background spectra. Signal (dashed) and background (solid) prompt spectra are shown through selection cuts described in the text. Background is primarily produced by cosmogenic fast neutrons. (Bottom) Simulated AD-I IBD signal (red) and background (blue) spectra after all analysis cuts. Signal-to-background of better than 1:1 is predicted. The rate and shape of the residual IBD-like background can be measured with high precision during reactor off periods.

Cuts	IBD signal	Cosmic BG
PSD	1630	2.1e6
Time (1, 2, 3)	1570	3.4e4
Spatial (4, 5)	1440	9900
Fiducial (6)	660	250

TABLE III. Simulated signal and cosmic background rates in events per day in the energy range  $0.8 \leq E \leq 7.2\ \text{MeV}$ , after applying background rejection cuts.

must be isolated from other neutron recoils or captures in a  $\pm 250\ \mu\text{s}$  window, to reject multi-neutron spallation showers. “Spatial topology” cuts include: (4) the prompt and delayed signals must be proximate; (5) multiple segment hits in the prompt signal must be distributed over a compact volume, rejecting extended minimum ionizing tracks and many high-energy gammas; (6) events occurring outside the inner fiducial volume ( $\geq$  one segment width from any active volume surface) are vetoed.

Although fiducialization decreases the effective active volume for true IBDs by  $\sim 50\%$ , it provides a more

than tenfold boost in background rejection. Predicted rates with cuts are given in Table III. Within the fiducialized volume, IBD detection efficiency is 42%. Efficiencies for the fiducial segments are largely consistent: a percent-level  $1\sigma$  deviation in efficiencies between segments can be corrected for in an oscillation analysis utilizing gamma and neutron calibration results. Monte Carlo investigations have also characterized the small expected geometry-induced spectral differences between segments within the fiducialized volume.

While event selection is not yet optimized, the signal-to-background ratio indicated is more than sufficient to meet the PROSPECT physics goals (Sec. III A). Although the background prediction is inherently uncertain (estimated to be accurate within a factor of 2), we are confident likely gains from optimization will ensure that PROSPECT can successfully control backgrounds. The simulated background spectrum shown in Fig. 20(b) is used in the sensitivity calculations described in Sec. III. Reactor-off periods will be used to measure the background spectrum directly.

### C. Backgrounds from Internal Radioactivity

Internal contamination of trace radioactivity can introduce backgrounds that cannot be effectively removed through fiducialization. These predominantly consist of  $^{40}\text{K}$  and the uranium and thorium decay chains. Work has been done to identify radio-clean materials well-suited for installation in the detector package. Acrylic and other plastic polymers have largely been demonstrated to be low-background by many experiments, including Daya Bay and other  $\theta_{13}$  experiments. The internal reflectors are designed to be low-mass and will mainly consist of carbon fiber, another established low-background material. Radioactivity from the PMTs will be mitigated by a combination of passively moderating light guides and active fiducialization along a segment's length.

Few decays produce correlated signals that can mimic the IBD event signature: electron-recoil like prompt event with a delayed neutron capture. However, correlated  $^{214}\text{Bi} \rightarrow ^{214}\text{Po} \rightarrow ^{210}\text{Pb}$  decays in the  $^{238}\text{U}$  decay chain are one of them. Bi-Po decays consist of a beta-decay with endpoint of approximately 3 MeV followed by a 7.8 MeV alpha decay with a half-life of 164  $\mu\text{s}$ . Data collected with PROSPECT-20 at HFIR, shown in Fig. 21, demonstrate how Bi-Po decays appear in the PROSPECT data stream.

A rate of Bi-Po events of  $3.0 \pm 0.15$ /day/liter was observed with the delayed alpha's quenched light output of 0.89 MeV $_{ee}$ . With the demonstrated energy resolution of the internal-reflector phase of PROSPECT-20, the alpha peak will be well-separated from the (n,Li) capture peak, eliminating greater than 99.5% of the Bi-Po events while preserving greater than 99% of neutron captures. Applying this rejection power, the Bi-Po signal is re-

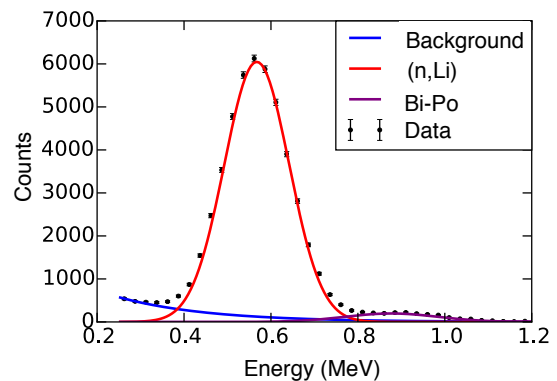


FIG. 21. Fitted distribution of delayed energy depositions in the PROSPECT-20 detector collected at HFIR. The main peak is from neutron captures on  $^6\text{Li}$ , while the smaller peak at 0.89 MeV is from Bi-Po alpha decays. With demonstrated improvements in energy resolution, these peaks will be completely separated in PROSPECT

duced to approximately 30/day, an order of magnitude below the IBD rate.

## VI. Conclusions

Since their first observation some 60 years ago, reactor antineutrinos have been an excellent tool for the study of neutrinos and neutrino oscillation. As an experiment at very short baselines from a research reactor with a highly-enriched uranium core, PROSPECT will make a precise measurement of the reactor antineutrino spectrum from  $^{235}\text{U}$  with an energy resolution of better than 4.5% at the High Flux Isotope Reactor at ORNL and search for neutrino oscillations as a sign of eV-scale sterile neutrinos. Utilizing a single, segmented 3-ton liquid scintillator detector located at 7–12 m from the reactor core, PROSPECT Phase I will probe the favored region of parameter space at  $>3\sigma$  within 3 years of data taking. Phase II will add a second detector with  $\sim 10$ -tons active target mass and cover the majority of the allowed parameter space at  $>5\sigma$ . PROSPECT has performed extensive R&D on detector components and built and operated a series of test detectors with increasing size. These test detectors have allowed the characterization and validation of the detector design as well as background studies in the reactor environment at HFIR. PROSPECT is technically ready to proceed with the construction of Phase I of the experiment and a first physics result can be obtained within 1 year of data taking.

## VII. Acknowledgements

This material is based upon work supported by the U.S. Department of Energy Office of Science. Additional support for this work is provided by Yale Univer-

sity, the Illinois Institute of Technology, the National Institute of Standards and Technology, and the Lawrence Livermore National Laboratory LDRD program. We gratefully acknowledge the support and hospitality of the High Flux Isotope Reactor and the Physics Division at Oak Ridge National Laboratory, managed by UT-Battelle for the U.S. Department of Energy.

- 
- [1] T. Mueller *et al.*, Phys. Rev. **C83**, 054615 (2011), arXiv:1101.2663 [hep-ex].
- [2] P. Huber, Phys. Rev. **C84**, 024617 (2011), arXiv:1106.0687 [hep-ph].
- [3] G. Mention *et al.*, Phys. Rev. **D83**, 073006 (2011), arXiv:1101.2755 [hep-ex].
- [4] K. Abazajian, M. Acero, S. Agarwalla, A. Aguilar-Arevalo, C. Albright, *et al.*, (2012), arXiv:1204.5379 [hep-ph].
- [5] J. Kopp, P. A. N. Machado, M. Maltoni, and T. Schwetz, JHEP **1305**, 050 (2013), arXiv:1303.3011 [hep-ph].
- [6] F. P. An *et al.* (Daya Bay), (2015), arXiv:1508.04233 [hep-ex].
- [7] Y. Abe *et al.* (Double Chooz), JHEP **10**, 086 (2014), [Erratum: JHEP02,074(2015)], arXiv:1406.7763 [hep-ex].
- [8] S.-B. Kim, *Proceedings, Neutrino Oscillation Workshop (NOW 2014)*, Nucl. Part. Phys. Proc. **265-266**, 93 (2015), arXiv:1412.2199 [hep-ex].
- [9] *PROSPECT website*, <http://prospect.yale.edu>.
- [10] R. Gandhi, B. Kayser, M. Masud, and S. Prakash, (2015), arXiv:1508.06275 [hep-ph].
- [11] F. Capozzi, E. Lisi, and A. Marrone, (2015), arXiv:1508.01392 [hep-ph].
- [12] *High Flux Isotope Reactor*, <https://neutrons.ornl.gov/hfir>.
- [13] *Oak Ridge National Laboratory*, <https://www.ornl.gov>.
- [14] H. Kwon *et al.* (ILL Collaboration), Phys. Rev. **D24**, 1097 (1981).
- [15] G. Zacek *et al.* (CALTECH-SIN-TUM), Phys. Rev. **D34**, 2621 (1986).
- [16] G. S. Vidyakin *et al.* (Krasnoyarsk), Sov. Phys. JETP **66**, 243 (1987), [Zh. Eksp. Teor. Fiz.93,424(1987)].
- [17] A. I. Afonin *et al.* (Rovno), Sov. Phys. JETP **67**, 213 (1988), [Zh. Eksp. Teor. Fiz.94N2,1(1988)].
- [18] A. A. Kuvshinnikov *et al.* (Rovno), JETP Lett. **54**, 253 (1991), [Sov. J. Nucl. Phys.52,300(1990)].
- [19] Y. Declais, J. Favier, A. Metref, H. Pessard, B. Achkar, *et al.*, Nucl.Phys. **B434**, 503 (1995).
- [20] Y. Declais *et al.* (Bugey), Phys. Lett. **B338**, 383 (1994).
- [21] G. S. Vidyakin *et al.* (Krasnoyarsk), JETP Lett. **59**, 390 (1994), [Pisma Zh. Eksp. Teor. Fiz.59,364(1994)].
- [22] Z. D. Greenwood *et al.* (SRP), Phys. Rev. **D53**, 6054 (1996).
- [23] K. Schreckenbach, G. Colvin, W. Gelletly, and F. Von Feilitzsch, Phys. Lett. **B160**, 325 (1985).
- [24] A. Hahn *et al.*, Phys. Lett. **B218**, 365 (1989).
- [25] K. Schreckenbach, F. H.R., F. Von Feilitzsch, H. A.A., *et al.*, Phys. Lett. **B99**, 251 (1981).
- [26] F. Von Feilitzsch, A. Hahn, and K. Schreckenbach, Phys. Lett. **B118**, 162 (1982).
- [27] K. Olive *et al.* (Particle Data Group), Chin. Phys. C **38**, 090001 (2014).
- [28] A. C. Hayes *et al.*, Phys. Rev. Lett. **112**, 202501 (2014), arXiv:1309.4146 [nucl-th].
- [29] A. C. Hayes *et al.*, (2015), arXiv:1506.00583 [nucl-th].
- [30] A. A. Zakari-Issoufou *et al.* (IGISOL), Phys. Rev. Lett. **115**, 102503 (2015), arXiv:1504.05812 [nucl-ex].
- [31] N. Haag *et al.*, Phys. Rev. Lett. **112**, 122501 (2014), arXiv:1312.5601 [nucl-ex].
- [32] D. A. Dwyer and T. J. Langford, Phys. Rev. Lett. **114**, 012502 (2015), arXiv:1407.1281 [nucl-ex].
- [33] B. C. Rasco *et al.*, *Proceedings, 2nd Conference on Advances in Radioactive Isotope Science (ARIS2014)*, JPS Conf. Proc. **6**, 030018 (2015).
- [34] P. Anselmann *et al.* (GALLEX), Phys. Lett. **B342**, 440 (1995).
- [35] W. Hampel *et al.* (GALLEX), Phys. Lett. **B420**, 114 (1998).
- [36] J. Abdurashitov *et al.* (SAGE), Phys. Rev. **C59**, 2246 (1999), arXiv:hep-ph/9803418 [hep-ph].
- [37] J. Abdurashitov, V. Gavrin, S. Girin, V. Gorbachev, P. Gurkina, *et al.*, Phys. Rev. **C73**, 045805 (2006), arXiv:nucl-ex/0512041 [nucl-ex].
- [38] A. Aguilar-Arevalo *et al.* (LSND), Phys. Rev. **D64**, 112007 (2001), arXiv:hep-ex/0104049 [hep-ex].
- [39] A. Aguilar-Arevalo *et al.* (MiniBooNE), Phys. Rev. Lett. **110**, 161801 (2013), arXiv:1207.4809 [hep-ex].
- [40] C. Giunti, M. Laveder, Y. Li, and H. Long, Phys. Rev. **D88**, 073008 (2013), arXiv:1308.5288 [hep-ph].
- [41] C. Giunti and E. M. Zavanin, (2015), arXiv:1511.03838 [hep-ph].
- [42] Nuclear Science Advisory Committee (NSAC), *Reaching for the Horizon: The 2015 NSAC Long Range Plan* (2015), [http://science.energy.gov/~media/np/nsac/pdf/2015LRP/2015\\_LRPNS\\_091815.pdf](http://science.energy.gov/~media/np/nsac/pdf/2015LRP/2015_LRPNS_091815.pdf).
- [43] J. Formaggio and J. Barrett, Physics Letters B **706**, 68 (2011).
- [44] A. Esmaili and O. L. G. Peres, Phys. Rev. D **85**, 117301 (2012).
- [45] P. A. R. Ade *et al.* (Planck), (2015), arXiv:1502.01589 [astro-ph.CO].
- [46] S. Gariazzo, C. Giunti, and M. Laveder, (2014), arXiv:1404.6160 [astro-ph.CO].
- [47] N. Ryder (SoLid), in *Proceedings, 2015 European Physical Society Conference on High Energy Physics (EPS-HEP 2015)* (2015) arXiv:1510.07835 [hep-ex].
- [48] I. Alekseev *et al.*, Phys. Part. Nucl. Lett. **11**, 473 (2014), arXiv:1305.3350 [physics].
- [49] A. P. Serebrov *et al.*, J. Exp. Theor. Phys. **121**, 578 (2015), [Zh. Eksp. Teor. Fiz.148,no.4,665?674(2015)].
- [50] M. Pequignot (Stereo, Nucifer), *Proceedings, Neutrino Oscillation Workshop (NOW 2014)*, Nucl. Part. Phys. Proc. **265-266**, 126 (2015).
- [51] B. R. Kim *et al.*, (2015), arXiv:1511.05551 [physics.ins-det].

- [52] C. Lane *et al.*, (2015), arXiv:1501.06935 [physics.ins-det].
- [53] G. Bellini *et al.* (Borexino), JHEP **1308**, 038 (2013), arXiv:1304.7721 [physics.ins-det].
- [54] J. Ashenfelter *et al.* (PROSPECT), Nucl. Instrum. Meth. **A806**, 401 (2016), arXiv:1506.03547 [physics.ins-det].
- [55] M. Antonello *et al.* (LAr1-ND, ICARUS-WA104, Micro-BooNE), (2015), arXiv:1503.01520 [physics.ins-det].
- [56] K. Heeger, B. Littlejohn, and H. Mumm, (2013), arXiv:1307.2859 [hep-ex].
- [57] F. P. An *et al.* (Daya Bay), Phys. Rev. Lett. **113**, 141802 (2014).
- [58] K. Heeger, B. Littlejohn, H. Mumm, and M. Tobin, Phys. Rev. **D87**, 073008 (2013), arXiv:1212.2182 [hep-ex].
- [59] J. Ashenfelter *et al.* (PROSPECT), in *Community Summer Study 2013: Snowmass on the Mississippi (CSS2013) Minneapolis, MN, USA, July 29-August 6, 2013* (2013) arXiv:1309.7647 [physics.ins-det].
- [60]  $F(E_{\bar{\nu}}) = \exp(\sum_i \alpha_i E_{\bar{\nu}}^{i-1})$ , with  $\alpha = \{1.418, -0.6078, 8.955 \times 10^{-3}, -6.690 \times 10^{-3}, 6.933 \times 10^{-5}\}$ .
- [61] P. Boczar, in *Nuclear Fuel Cycle Science and Engineering*, Woodhead Publishing Series in Energy, edited by I. Crossland (Woodhead Publishing, 2012) pp. 278 – 299.
- [62] D. Torgerson, B. A. Shalaby, and S. Pang, Nuclear Engineering and Design **236**, 1565 (2006).
- [63] A. Bernstein, Y.-F. Wang, G. Gratta, and T. West, J. Appl. Phys. **91**, 4672 (2002), arXiv:nucl-ex/0108001 [nucl-ex].
- [64] A. Bernstein *et al.*, Science and Global Security **18**, 127 (2010), nucl-ex/0908.4338.
- [65] G. Jocher *et al.*, Phys. Rept. **527**, 131 (2013), 1307.2832.
- [66] IAEA, *Final Report of the Focused Workshop on Antineutrino Detection for Safeguards Applications* (2009), sTR-361.
- [67] IAEA, *Proceedings of the first meeting of the Ad Hoc Working Group on Safeguards Applications utilizing Antineutrino Detection and Monitoring* (2012), sG-EQ-GNRL-RP-0002.
- [68] B. Achkar *et al.*, Nuclear Physics B **434**, 503 (1995).
- [69] Eljen EJ-309 Liquid Scintillator, <http://www.eljentechnology.com/index.php/products/liquid-scintillators/73-ej-309>.
- [70] M. Gordon *et al.*, IEEE Trans. Nucl. Sci. **51**, 3427 (2004).
- [71] M. Kowatari *et al.*, J. Nucl. Sci. Technol. **42**, 495 (2005).
- [72] PerkinElmer UltimaGold AB Liquid Scintillator, <http://www.perkinelmer.com/catalog/family/id/ultima+gold+ab>.
- [73] J. Ashenfelter *et al.* (PROSPECT), JINST **10**, P11004 (2015), arXiv:1508.06575 [physics.ins-det].
- [74] Hamamatsu Photomultiplier Tubes and Assemblies, [http://www.hamamatsu.com/resources/pdf/etd/High\\_energy\\_PMT\\_TPM00007E.pdf](http://www.hamamatsu.com/resources/pdf/etd/High_energy_PMT_TPM00007E.pdf).
- [75] 3M ESR Datasheet, <http://multimedia.3m.com/mws/media/3808020/vikuititm-esr-msds.pdf?fn=ESR.pdf>.
- [76] WaterBrick International, <http://www.waterbrick.org>.
- [77] S. Agostinelli *et al.* (GEANT4), Nucl. Instrum. Methods **A506**, 250 (2003).
- [78] C. Hagmann, D. Lange, and D. Wright, in *Nuclear Science Symposium Conference Record*, Vol. 2 (IEEE, 2007) pp. 1143–1146.
- [79] T. Sato and K. Niita, Radiat. Res. **166**, 544 (2006).
- [80] Slitrani Optical Simulation Package, <http://gentitfx.fr/SLitrani/>.
- [81] M. Abbes *et al.*, Nucl. Instrum. Methods **A374**, 164 (1996).